Finite-field implementation of NMR chemical shieldings for molecules: Direct and converse gauge-including projector-augmented-wave methods

Filipe Vasconcelos, Gilles A. de Wijs, Remco W. A. Havenith, Martijn Marsman, and Georg Kresse

Articles you may be interested in

Four-component relativistic theory for nuclear magnetic shielding: Magnetically balanced gauge-including atomic orbitals
J. Chem. Phys. **131**, 244113 (2009); 10.1063/1.3283036

Relativistic calculation of nuclear magnetic shielding tensor using the regular approximation to the normalized elimination of the small component. III. Introduction of gauge-including atomic orbitals and a finite-size nuclear model
J. Chem. Phys. **129**, 224103 (2008); 10.1063/1.3028047

Relaxed core projector-augmented-wave method
J. Chem. Phys. **125**, 104101 (2006); 10.1063/1.2338035

Quasirelativistic theory for magnetic shielding constants. II. Gauge-including atomic orbitals and applications to molecules
J. Chem. Phys. **118**, 1027 (2003); 10.1063/1.1528934

Natural chemical shielding analysis of nuclear magnetic resonance shielding tensors from gauge-including atomic orbital calculations
J. Chem. Phys. **107**, 1173 (1997); 10.1063/1.474464

Finite-field implementation of NMR chemical shieldings for molecules: Direct and converse gauge-including projector-augmented-wave methods

Filipe Vasconcelos,[1,a)] Gilles A. de Wijs,[1,b)] Remco W. A. Havenith,[2] Martijn Marsman,[3] and Georg Kresse[3]

[1]*Institute for Molecules and Materials, Radboud University, Heyendaalseweg 135, NL-6525 AJ Nijmegen, The Netherlands*
[2]*Zernike Institute for Advanced Materials, Rijksuniversiteit Groningen, Nijenborgh 4, NL-9747 AG Groningen, The Netherlands*
[3]*Department of Computational Materials Physics, University of Vienna, Sensengasse 8/12, A-1060 Wien, Austria*

Two finite-field implementations for the calculation of chemical shieldings of molecular systems using a plane-wave basis set and the Gauge-Including Projector-Augmented-Wave method are presented. The direct approach mimics the nuclear magnetic resonance experiment in that it puts the molecule in a uniform magnetic field and obtains shieldings from the current response. The other is based on the recently introduced "converse method" [T. Thonhauser, D. Ceresoli, A. A. Mostofi *et al.*, J. Chem. Phys. **131**, 101101 (2009)]. In both methods two-center contributions to the shieldings can be included via a numerically simple augmentation construction. Results obtained with both methods are discussed as well as (dis)similarities in their behaviors. © *2013 AIP Publishing LLC*.
[http://dx.doi.org/10.1063/1.4810799]

I. INTRODUCTION

Nuclear magnetic resonance (NMR) spectroscopy is a powerful tool to study the structure of molecules, liquids, and solids. One of the key parameters determining the spectrum is the chemical shielding tensor $\sigma_{\mathbf{R}\alpha\beta}$,[1,2] defined as

$$\sigma_{\mathbf{R}\alpha\beta} = -\frac{\partial B_{\mathbf{R}\alpha}^{\text{ind}}}{\partial B_{\beta}^{\text{ext}}}, \quad (1)$$

where $B_{\mathbf{R}\alpha}^{\text{ind}}$ is the induced magnetic field at a specific atomic nucleus $\mathbf{R}$ when an external field B_{β}^{ext} is applied (α and β denote Cartesian directions). Retrieving the structural information from the measured shielding in general is a complicated process, as there exists no simple direct mapping from shielding to structure. Solving this issue has motivated the development of *ab initio* and first-principles techniques to calculate shieldings.

Calculation of chemical shieldings for molecular systems is now a mature discipline in quantum chemistry (see, e.g., Ref. 3 and references therein), for wave function methods as well as Density Functional Theory (DFT) methods. As crystalline systems pose additional challenges first-principles DFT methods for solids have been developed somewhat later. The fundamental problem of dealing with a finite applied field in a periodically repeated system was solved by Mauri, Pfrommer, and Louie in the 1990s, using linear-response (LR) in the long wave-length limit.[4] Later, an alternative route was developed by Sebastiani and Parrinello.[5] Furthermore, Gregor, Mauri, and Car showed that the shielding due to core

electrons can be considered rigid, i.e., can be calculated separately, when adopting an appropriate gauge for the vector potential.[6] This solved a major practical problem because many solid state codes remove the core states from the calculation. An important breakthrough occurred with the introduction of the Gauge-Including Projector Augmented Wave (GIPAW) method by Pickard and Mauri.[7] The GIPAW method permits to obtain accurate chemical shielding with a plane-wave (PW) basis set. It recovers the shape of the all-electron Kohn-Sham (KS) orbitals near the nucleus via an augmentation procedure as in Blöchl's Projector Augmented Wave (PAW) method.[8] Moreover, it solves the gauge problem arising from incompleteness of the atom-centered augmentation functions in a way similar as done for molecules in the Gauge Independent Atomic Orbital (GIAO) method.[9] The extension to non-norm-conserving pseudo orbitals in the PAW was done by Yates, Pickard, and Mauri (YPM).[10] The complete methodology resulting from these developments, often just called "GIPAW method," has been implemented in several plane-wave codes and is currently widely used in the solid-state NMR community for an extensive range of applications (see, e.g., Ref. 11 and references therein). Recently also an extension of the linear response formalism for solids to GIAO and Augmented-Plane-Wave (APW) methods has been realized.[12–14]

All these are *direct* methods, i.e., they mimic the physics of the NMR experiment: The material is put in a uniform external field $\mathbf{B}^{\text{ext}}$, the induced current is calculated, and from that the induced field $\mathbf{B}_{\mathbf{R}}^{\text{ind}}$ at the atomic nucleus is obtained. Recently, a new method to calculate chemical shieldings was introduced by Thonhauser *et al.*,[15] building on important developments in the theory of orbital magnetization of crystals.[16] This *converse* approach exploits a different

physical setting. The shielding tensor $\sigma_{\mathbf{R}\alpha\beta}$ is calculated from the induced orbital moment $\mathbf{m}^{\text{ind}}$ when an external ideal magnetic dipole $\mathbf{m}^{\text{ext}}$ is placed on a specific nucleus $\mathbf{R}$,[15] from the formula:

$$-\frac{\partial B_{\mathbf{R}\alpha}^{\text{ind}}}{\partial B_{\beta}^{\text{ext}}} = \sigma_{\mathbf{R}\alpha\beta} = -\frac{\partial m_{\beta}^{\text{ind}}}{\partial m_{\mathbf{R}\alpha}^{\text{ext}}}. \qquad (2)$$

The left-hand-side expression is the usual definition of the shielding tensor in the direct approach, Eq. (1). To prove this expression one notes that the induced magnetic field can be written as minus the derivative of the (total) energy with respect to the magnetic moment (for vanishing moment), and that the induced magnetic moment can be written as minus the field derivative of the energy (for vanishing magnetic field):[17]

$$B_{\mathbf{R}\alpha}^{\text{ind}} = -\frac{\partial E}{\partial m_{\mathbf{R}\alpha}^{\text{ext}}} \quad \text{and} \quad m_{\beta}^{\text{ind}} = -\frac{\partial E}{\partial B_{\beta}^{\text{ext}}}. \qquad (3)$$

Contrary to the direct methods, in the converse approach a *local* perturbation is applied, and a *global* response results. Moreover, the response is calculated by directly applying a finite field, i.e., there is no need for a linear response calculation. This even holds for crystals, as the orbital moment of a crystal can be directly obtained from the Hamiltonian, eigenvalues and **k**-derivatives of the cell periodic part of the orbitals.[16] A first-principles solid-state converse method based on the GIPAW reconstruction of the valence states has been developed by Ceresoli, Marzari, Lopez, and Thonhauser (CMLT).[18] It has been implemented in QUANTUM-ESPRESSO (QE) (Ref. 19) and VASP (Vienna *ab initio* simulation package).[20,21] See, e.g., Refs. 22 and 23 for applications.

In this paper we apply the DFT GIPAW approach to molecular systems. The implementation discussed here is based on VASP. We report on both (a) a simple direct method and (b) a converse molecular method. In both approaches a finite field is applied directly. In this respect (a) differs from previous direct molecular GIPAW implementations all relying on linear response.[7,10] For (b) the converse GIPAW approach of CMLT (Ref. 18) is closely followed. However, here it is specifically geared towards usage for molecules, allowing for a straightforward and simple calculation of the moment of the plane-wave part of the current, avoiding the recurrence to the modern theory of orbital magnetization of Ref. 15. Moreover, we generalize the method to pseudo partial waves that are not normalized, and demonstrate the equivalence of both approaches.

Finally, for both methods, we provide a simple augmentation correction that accounts for two-center contributions to the shielding. Typically such corrections are small, and have hitherto been neglected in GIPAW implementations.[7,10] For hydrogen—having a very small range of shieldings—we show these corrections to be relevant for some applications.

We expect the implementation to be particularly relevant for larger molecular systems. For small systems quantum chemical codes using, e.g., Gaussian basis sets are much faster, since the plane wave basis sets are notoriously inefficient in the vacuum requiring an equally dense real space spacing there as close to the atom. However, for very large molecules, where the vacuum region takes up a smaller frac-

tion of the computational cell, the inefficiency of the plane-wave basis set is less acute and the good scaling of plane waves [up to 1000 atoms predominantly $N^2\log(N)$] makes plane waves competitive. Furthermore, the converse method allows to consider just a small fraction of the molecule (e.g., near the active site) as the effort scales linearly with the number of shielding tensors calculated. This feature carries over to molecular systems.

This paper is organized as follows: In Sec. II, we briefly review the general theory of the chemical shieldings for molecules using the direct and converse approaches. In Sec. III, the formulas within the GIPAW framework are summarized, together with details of the implementation in VASP. Section IV compares results for small molecules obtained with both molecular approaches, the linear response approach of Yates, Pickard, and Mauri (Ref. 10) as implemented in VASP and QUANTUM-ESPRESSO,[19] and the molecular linear response from DALTON.[24–26] This section also deals with numerical issues such as basis set convergence and convergence criteria for orbital optimization, and demonstrates the feasibility of the present approach for larger molecular systems. Section V concludes with a short summary.

II. THEORY

This section summarizes the general theoretical background related to the calculation of the chemical shielding tensor for both the direct and converse approaches in a basis-set independent "all-electron" picture. For both approaches we present the all-electron Hamiltonian and the respective induced quantities. Thereafter, we introduce the notation of the PAW and GIPAW transformation needed in Sec. III.

A. Hamiltonian and current operator

1. Hamiltonian

In the presence of a magnetic field the all-electron (AE) Hamiltonian H is given by

$$H = \frac{1}{2m_e}\left(\mathbf{p} - \frac{e}{c}\mathbf{A}\right)^2 + eV(\mathbf{r}), \qquad (4)$$

where $V(\mathbf{r})$ is the all-electron local potential, $\mathbf{p}$ is the momentum operator, and $e = -|e|$ is the electron charge. The vector potential $\mathbf{A}$ depends on the external field or perturbation.

2. Current density and current operator

The computation of the chemical shielding in both approaches requires computing the current density. It is a function of the position $\mathbf{r}$ and can be decomposed into para and diamagnetic contributions:

$$\mathbf{j}(\mathbf{r}) = \mathbf{j}_{\text{para}}(\mathbf{r}) + \mathbf{j}_{\text{dia}}(\mathbf{r}). \qquad (5)$$

The current densities are obtained from the respective current operators:

$$\mathbf{J}_{\text{para}} = \frac{e\hbar}{2im_e}\left(\boldsymbol{\nabla}\,|\mathbf{r}\rangle\langle\mathbf{r}| + |\mathbf{r}\rangle\langle\mathbf{r}|\,\boldsymbol{\nabla}\right), \qquad (6)$$

$$\mathbf{J}_{\text{dia}} = -\frac{e^2}{m_e c} \mathbf{A}(\mathbf{r}) |\mathbf{r}\rangle \langle \mathbf{r}|. \tag{7}$$

In a one-electron picture and for the Hamiltonian (4), the current densities are just a simple sum of expectation values:

$$\mathbf{j}_{\text{para}}(\mathbf{r}) = \frac{e\hbar}{m_e} \text{Im} \sum_n f_n [\psi_n^* \nabla \psi_n], \tag{8}$$

$$\mathbf{j}_{\text{dia}}(\mathbf{r}) = -\frac{e^2}{m_e c} \mathbf{A}(\mathbf{r}) \rho(\mathbf{r}), \tag{9}$$

where f_n are the occupation numbers (0 or 2) and $\rho(\mathbf{r})$ is the AE charge density.

3. Vector potential

For the vector potential $\mathbf{A}_0$ of the uniform, external magnetic field $\mathbf{B}$ we use

$$\mathbf{A}_0(\mathbf{r}) = \frac{1}{2}\mathbf{B} \times \mathbf{r}, \tag{10}$$

and for the vector potential $\mathbf{A}_s$ of an ideal dipole $\mathbf{m}_s$ at position $\mathbf{R}_s$ we use

$$\mathbf{A}_s = \frac{\mathbf{m}_s \times (\mathbf{r} - \mathbf{R}_s)}{|\mathbf{r} - \mathbf{R}_s|^3}. \tag{11}$$

Both vector potentials obey the Coulomb gauge condition $\nabla \cdot \mathbf{A} = 0$. In general, the vector potential is a sum of both: $\mathbf{A}(\mathbf{r}) = \mathbf{A}_0(\mathbf{r}) + \mathbf{A}_s(\mathbf{r})$, so the AE Hamiltonian is

$$H = \frac{1}{2m_e} \left[\mathbf{p} - \frac{e}{c}(\mathbf{A}_0(\mathbf{r}) + \mathbf{A}_s(\mathbf{r})) \right]^2 + eV(\mathbf{r}). \tag{12}$$

To first order in external moment and field it is

$$H = \frac{p^2}{2m_e} - \frac{e}{m_e c}(\mathbf{A}_0 + \mathbf{A}_s) \cdot \mathbf{p} + \frac{e^2}{m_e c^2}\mathbf{A}_0 \cdot \mathbf{A}_s + eV(\mathbf{r}). \tag{13}$$

B. Direct approach

1. Hamiltonian

We only apply a uniform field: $\mathbf{A}_s = 0$. To first order in the field, the AE Hamiltonian (Eq. (13)) is then:

$$H = \frac{p^2}{2m_e} - \frac{e}{m_e c}\mathbf{A}_0 \cdot \mathbf{p} + eV(\mathbf{r}). \tag{14}$$

2. Induced field

There are several ways to derive an expression for the induced field. In the traditional approach one uses the Biot-Savart law to calculate the (non-uniform) induced field from the induced current:

$$\mathbf{B}_{\text{ind}}(\mathbf{r}') = \frac{1}{c} \int \frac{\mathbf{j}_{\text{ind}}(\mathbf{r}) \times (\mathbf{r}' - \mathbf{r})}{|\mathbf{r}' - \mathbf{r}|^3} d^3 r. \tag{15}$$

The induced AE current $\mathbf{j}_{\text{ind}}$ is given by Eq. (5) with $\mathbf{A} = \mathbf{A}_0$. To obtain the shielding tensors, the field has to be calculated at the nuclear positions $\mathbf{R}$. If the perturbation is sufficiently

small the response is in the linear regime and

$$\sigma_{\mathbf{R}\alpha\beta} = -\frac{B_{\text{ind},\alpha}(\mathbf{R})}{B_\beta}. \tag{16}$$

An alternative route runs via the energy derivatives of Eq. (3), i.e., via the key observations of Thonhauser *et al.*[15] that underpin the formulation of the converse method, and the Hellmann-Feynman theorem:

$$B_{\mathbf{R}\alpha}^{\text{ind}} = -\frac{\partial E}{\partial m_{\mathbf{R}\alpha}^{\text{ext}}} = -\sum_n^{\text{occ}} f_n \langle \psi_n | \frac{\partial H}{\partial m_{\mathbf{R}\alpha}^{\text{ext}}} | \psi_n \rangle. \tag{17}$$

In the next step we have to determine the sum of the matrix elements $\langle \psi_n | H | \psi_n \rangle$. For H, we use Eq. (13) and retain only the terms linear in $\mathbf{A}_s$. We obtain

$$-\sum_n^{\text{occ}} f_n \langle \psi_n | -\frac{e}{m_e c}\mathbf{A}_s \cdot \mathbf{p} + \frac{e^2}{m_e c^2}\mathbf{A}_0 \cdot \mathbf{A}_s | \psi_n \rangle$$

$$= \mathbf{m}_s \cdot \frac{1}{c} \int \left(\frac{e\hbar}{im_e} \sum_n^{\text{occ}} f_n \psi_n^*(\mathbf{r}) \nabla \psi_n(\mathbf{r}) - \frac{e^2}{m_e c}\mathbf{A}_0(\mathbf{r})\rho(\mathbf{r}) \right)$$

$$\times \frac{(\mathbf{R}_s - \mathbf{r})}{|\mathbf{R}_s - \mathbf{r}|^3} d^3 r = \mathbf{m}_s \cdot \mathbf{B}_{\mathbf{R}_s}^{\text{ind}}.$$

Here, obviously, $\mathbf{R}_s = \mathbf{R}$. To derive this we had to insert $\mathbf{A}_s$ from Eq. (11) and reorder the vector and inner products. In the final expression one can clearly recognize the Biot-Savart law (Eq. (15)) and the current density (Eq. (5)) in uniform external field. We obtain $B_{\mathbf{R}\alpha}^{\text{ind}}$ by differentiating with respect to $m_{\mathbf{R}\alpha}^{\text{ext}}$.

C. Converse approach

1. Hamiltonian

A magnetic moment $\mathbf{m}_s$ is placed at the atomic position $\mathbf{R}_s$. There is no uniform external magnetic field: $\mathbf{A}_0 = 0$. The Hamiltonian of Eq. (13) simplifies and becomes:

$$H = \frac{p^2}{2m_e} - \frac{e}{m_e c}\mathbf{A}_s \cdot \mathbf{p} + eV(\mathbf{r}). \tag{18}$$

2. Induced moment

Analogous to the induced field in Sec. II B 2 above, there are again two ways to arrive at the induced moment.

(i)   Application of the external moment $\mathbf{m}_s$ gives rise to an induced current $\mathbf{j}_{\text{ind}}$ that is calculated from Eq. (5) with $\mathbf{A}(\mathbf{r}) = \mathbf{A}_s(\mathbf{r})$. In turn, this induced current gives the induced magnetic moment $\mathbf{m}_{\text{ind}}$. In a molecular set-up it is straightforwardly calculated using the definition of the orbital magnetic moment:

$$\mathbf{m}_{\text{ind}} = \frac{1}{2c} \int \mathbf{r} \times \mathbf{j}_{\text{ind}} d^3 r. \tag{19}$$

(ii)   Following CMLT,[18] one can also use Eq. (3) to obtain $\mathbf{m}_{ind}$ using the Hellmann-Feynman theorem:

$$\mathbf{m}_{in} = \Omega_c \mathbf{M}_{ind} = -\left\langle \frac{\partial H}{\partial \mathbf{B}} \right\rangle_{B=0}, \qquad (20)$$

(Ω_c is the cell volume). To do so, one needs to retain the vector potential $\mathbf{A}_0$ of the uniform field in the Hamiltonian, i.e., work with the full expression in Eq. (13). One obtains:

$$\mathbf{m}_{ind} = \frac{1}{2c} \int \mathbf{r}$$
$$\times \left(\frac{e\hbar}{im_e} \sum_n^{occ} f_n \psi_n^*(\mathbf{r}) \nabla \psi_n(\mathbf{r}) \right.$$
$$\left. - \frac{e^2}{m_e c} \mathbf{A}_s(\mathbf{r}) \rho(\mathbf{r}) \right) d^3 r,$$

in which Eq. (19) is easily recognized.

In an infinitely large crystal, Eq. (19) is not applicable and an alternative expression from the modern theory of orbital magnetization has to be used.[16, 18] In any case, the final shielding is:

$$\sigma_{\mathbf{R}_s \alpha \beta} = -\frac{m_{ind,\beta}}{m_{s\alpha}(\mathbf{R}_s)}. \qquad (21)$$

D. PAW and GIPAW methodologies

1. Basics of PAW

In Blöchl's PAW method (Ref. 8) the one-electron Kohn-Sham orbitals ψ_n are related to the pseudo orbitals $\tilde{\psi}_n$ via a linear transformation:

$$|\psi_n\rangle = |\tilde{\psi}_n\rangle + \sum_i (|\phi_i\rangle - |\tilde{\phi}_i\rangle)\langle \tilde{p}_i|\tilde{\psi}_n\rangle. \qquad (22)$$

The orbitals $\tilde{\psi}_n$, where n is the band index, are expanded in plane waves and represent the variational degrees of freedom. The all-electron partial waves ϕ_i are obtained from a reference atom calculation. They are stored as products of spherical harmonics and radial functions. The latter are tabulated on a logarithmic mesh, so as to allow for high accuracy in the immediate vicinity of the nucleus. The pseudo partial waves $\tilde{\phi}_i$ are equivalent to the all-electron partial waves outside the PAW spheres, and match continuously onto $\tilde{\phi}_i$ inside the PAW spheres. The projector functions $\tilde{p}_i$ are dual to the pseudo partial waves:

$$\langle \tilde{p}_i|\tilde{\phi}_j\rangle = \delta_{ij}. \qquad (23)$$

The PAW transform of any given quasi-local operator is given by

$$\tilde{O} = O + \sum_{ij} |\tilde{p}_i\rangle \left(D_{ij}^1[O] - \tilde{D}_{ij}^1[O] \right) \langle \tilde{p}_j|, \qquad (24)$$

where

$$D_{ij}^1[O] = \langle \phi_i|O|\phi_j\rangle \quad \text{and} \quad \tilde{D}_{ij}^1[O] = \langle \tilde{\phi}_i|O|\tilde{\phi}_j\rangle \qquad (25)$$

defines the strength parameter as introduced in Ref. 27. Here O is the AE operator and $\tilde{O}$ is the corresponding operator in the plane wave basis, i.e., for the expectation value:

$$\langle O \rangle = \sum_n f_n \langle \psi_n| O |\psi_n\rangle = \sum_n f_n \langle \tilde{\psi}_n| \tilde{O} |\tilde{\psi}_n\rangle$$
$$= \sum_n f_n \langle \tilde{\psi}_n| O |\tilde{\psi}_n\rangle + \rho_{ij} \left(D_{ij}^1[O] - \tilde{D}_{ij}^1[O] \right)$$

here f_n and ρ_{ij} are the band and the augmentation occupancies, respectively, with

$$\rho_{ij} = \sum_n f_n \langle \tilde{\psi}_n|\tilde{p}_i\rangle\langle \tilde{p}_j|\tilde{\psi}_n\rangle. \qquad (26)$$

The expectation value is calculated as the sum of the expectation value of the AE operator taken with the pseudo orbitals and one-center corrections.

We use periodic boundary conditions and a plane wave basis set for the pseudo orbitals:

$$\tilde{\psi}_{n,\mathbf{k}}(\mathbf{r}) = \frac{1}{N_k} \sum_{\mathbf{G},\mathbf{k}} c_{n,\mathbf{k}}^{\mathbf{G}} e^{i(\mathbf{k}+\mathbf{G})\cdot\mathbf{r}}. \qquad (27)$$

Here, $\mathbf{G}$ are the reciprocal lattice vectors of the applied unit cell and $\mathbf{k}$ labels the $\mathbf{k}$-points. Brillouin zone sampling is artificial in a molecular system, but a judicious choice may speed up convergence with cell size. However, all results reported were obtained using the Γ-point only.

2. Basics of GIPAW

The GIPAW transform was introduced by Pickard and Mauri to restore the correct phase change when a system is translated in a uniform magnetic field.[7] The need for such a transform is dictated by the observation that in the presence of a linearly increasing vector potential $\mathbf{A}_0$ (i.e., in constant magnetic field with gauge of Eq. (10)), the groundstate orbitals acquire an additional phase factor upon translation over a vector $\mathbf{t}$:

$$\tilde{\psi}_{n,\mathbf{k}}(\mathbf{r}) \rightarrow e^{(ie/\hbar c)\mathbf{A}_0(\mathbf{t})\cdot\mathbf{r}} \tilde{\psi}_{n,\mathbf{k}}(\mathbf{r}-\mathbf{t}). \qquad (28)$$

The exponent describes a rapid oscillation in space that cannot be properly sampled by the usual projectors, however, the on-site "Gauge" transformation of the GIPAW effectively cancels the phase oscillation in the pseudo orbitals, and allows the use of a modest number of partial waves and projectors.

In the GIPAW, the partial waves and projector functions hence receive an additional "phase twist." The phase twisted operators (denoted here by an additional bar) are related to the PAW operators as

$$\langle \bar{\phi}_i| = \langle \phi_i| e^{(-ie/\hbar c)\mathbf{A}_0(\mathbf{R})\cdot\mathbf{r}},$$
$$\langle \bar{\tilde{\phi}}_i| = \langle \tilde{\phi}_i| e^{(-ie/\hbar c)\mathbf{A}_0(\mathbf{R})\cdot\mathbf{r}}, \qquad (29)$$
$$\langle \bar{\tilde{p}}_i| = \langle \tilde{p}_i| e^{(-ie/\hbar c)\mathbf{A}_0(\mathbf{R})\cdot\mathbf{r}}.$$

Here $\mathbf{A}_0(\mathbf{R})$ is the vector potential of the magnetic field at the center of the PAW sphere: $\mathbf{A}_0(\mathbf{R}) = (\mathbf{B} \times \mathbf{R})/2$. Defining phase twisted strength parameters and projector functions, the GIPAW transform can be written just as compact as Eq. (24), i.e.,

$$\tilde{O} = O + \sum_{ij} |\bar{\tilde{p}}_i\rangle \left(\bar{D}_{ij}^1[O] - \bar{\tilde{D}}_{ij}^1[O] \right) \langle \bar{\tilde{p}}_j|. \qquad (30)$$

Here the projector functions are phase twisted ("outer operator" twist). The modified strength parameters have the AE operator phase twisted ("inner operator" twist):

$$\bar{D}_{ij}^1[O] = \langle \phi_i | e^{(-ie/\hbar c)\mathbf{A}_0(\mathbf{R})\cdot\mathbf{r}} O e^{(ie/\hbar c)\mathbf{A}_0(\mathbf{R})\cdot\mathbf{r}} | \phi_j \rangle . \quad (31)$$

Note that the seemingly different sign in comparison with YPM and CMLT is due to a difference in the sign of charge.[7,10,18] In the following we always use a "bar" to denote phase twisted quantities, e.g.,

$$\bar{\rho}_{ij} = \sum_n f_n \langle \tilde{\psi}_n | \bar{\tilde{p}}_i \rangle \langle \bar{\tilde{p}}_j | \tilde{\psi}_n \rangle . \quad (32)$$

The GIPAW largely removes the gauge problem in the one-center augmentation. It effectively shifts the gauge origin to the center of each PAW sphere (see below).

If the plane wave basis is sufficiently large, the variation of the pseudo orbitals introduced by the linearly increasing vector potential can be described exactly ($e^{(ie/\hbar c)\mathbf{A}_0(\mathbf{t})\cdot\mathbf{r}}$ has the form of a plane wave) although effectively reducing the plane wave cutoff by $\propto (ie/\hbar c)\mathbf{A}_0(\mathbf{t})$.

We use the same projector functions and partial waves for both GIPAW and PAW calculations. The difference is just in applying the phase twists.

III. MOLECULAR GIPAW METHODS

This section provides expressions for the GIPAW Hamiltonians and the induced response properties, i.e., magnetic field and moment for the two methods, respectively. In the present implementation, we compute the response by applying a finite field: in the direct method, a finite magnetic field is applied and the induced field at each nucleus is determined, whereas for the converse method, a finite magnetic dipole is placed at a specific nuclear position, and the induced current and moment are calculated.

A. Direct approach

The use of a finite magnetic field **B** with a corresponding vector potential $\mathbf{A}_0$ according to Eq. (10), is obviously inconsistent with the periodic boundary conditions. To remedy this we apply a saw-tooth vector potential. The molecule is located at the origin, and in the vacuum, ideally where the electronic density becomes minimal, the potential makes a jump (we apply the jump half-way the cell, see Fig. 1). This jump is smoothed in order to avoid unwanted artifacts in the fast Fourier transforms. The corresponding magnetic field is consistent with periodic boundary conditions, and we chose it such that the average field is zero (**G** = 0 component).

1. GIPAW Hamiltonian

Here we describe the modifications of the Hamiltonian when the saw-tooth vector potential is switched on. In zero external field the usual PAW Hamiltonian (Eq. (47) of
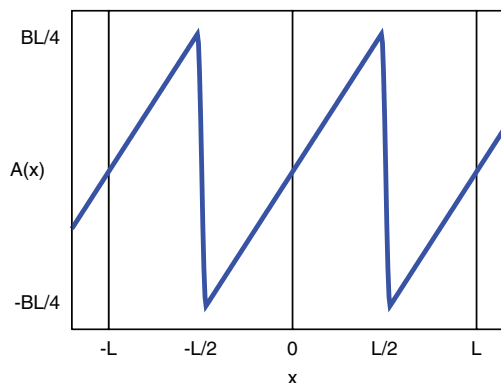

FIG. 1. One-dimensional representation of the vector potential in a supercell of size L. Due to the vector potential discontinuity in the middle of the box, the center of mass of the target molecule should be placed at the origin.

Ref. 27) and overlap operator apply:

$$H^{\text{PAW}} = \frac{p^2}{2m} + \tilde{v}_{\text{eff}} + \sum_{\mathbf{R}ij} |\tilde{p}_{\mathbf{R}i}\rangle \left(\hat{D}_{ij} + D_{ij}^1 - \tilde{D}_{ij}^1 \right) \langle \tilde{p}_{\mathbf{R}j}|$$

and

$$S^{\text{PAW}} = \sum_{\mathbf{R}ij} |\tilde{p}_{\mathbf{R}i}\rangle Q_{ij} \langle \tilde{p}_{\mathbf{R}j}| . \quad (33)$$

See Ref. 27 for a more detailed discussion of the individual terms. Switching on the field, all projection operators in H^{PAW} and S^{PAW} become gauge twisted, i.e., $\tilde{p}_i \rightarrow \bar{\tilde{p}}_i$ (we apply the projectors in real space, Ref. 28). Inclusion of the vector potential $\mathbf{A}_0(\mathbf{r})$ (cf. Eq. (14)) yields the total GIPAW Hamiltonian

$$H^{\text{GIPAW}}$$
$$= \bar{H}^{\text{PAW}} - \frac{e}{m_e c}\mathbf{A}_0(\mathbf{r}) \cdot \mathbf{p} - \frac{e}{m_e c} \sum_{\mathbf{R}ij} |\bar{\tilde{p}}_{\mathbf{R}i}\rangle$$
$$\left(D_{\mathbf{R}ij}^1[\mathbf{A}_0(\mathbf{r}-\mathbf{R})\cdot\mathbf{p}] - \tilde{D}_{\mathbf{R}ij}^1[\mathbf{A}_0(\mathbf{r}-\mathbf{R})\cdot\mathbf{p}] \right) \langle \bar{\tilde{p}}_{\mathbf{R}j}| .$$
$$(34)$$

Here $\bar{H}^{\text{PAW}}$ is the original Hamiltonian of Eq. (33) without field but with gauge twisted projectors. As discussed before, the gauge twisted projectors move the origin of the vector field in the one-center terms to the origin of each PAW sphere. Here we explicitly label the PAW spheres with **R**.

2. Total induced field

There are several routes leading to $\mathbf{B}_{\text{ind}}(\mathbf{R}')$, i.e., the induced magnetic field at nucleus $\mathbf{R}'$. First, we briefly outline the direct route via Eqs. (3) and (17). In this case we start with an AE Hamiltonian, Eq. (12), with both the uniform magnetic field (vector potential $\mathbf{A}_0$) and a magnetic dipole placed at nucleus of interest (vector potential $\mathbf{A}_s$ with $\mathbf{R}_s = \mathbf{R}'$). With help of the Hellmann-Feynman theorem the induced field is

$$\mathbf{B}_{\text{ind}}(\mathbf{R}') = -\frac{\partial E}{\partial \mathbf{m}_{\mathbf{R}'}^{\text{ext}}} = -\sum_n^{\text{occ}} f_n \langle \tilde{\psi}_n | \frac{\partial \tilde{H}}{\partial \mathbf{m}_s} | \tilde{\psi}_n \rangle_{\mathbf{m}_s=0} .$$

Here $\tilde{H}$ denotes the GIPAW transform of the AE Hamiltonian. There are no overlap and double counting terms because

they are not explicitly dependent on $\mathbf{m}_s$. $\mathbf{B}_{ind}(\mathbf{R}')$ consist of a (pseudo) contribution that is calculated on the grid and one-center corrections:

$$\mathbf{B}_{ind}(\mathbf{R}') = \tilde{\mathbf{B}}_{ind}(\mathbf{R}') + \tilde{\mathbf{B}}^1_{ind}(\mathbf{R}') - \mathbf{B}^1_{ind}(\mathbf{R}').$$

The first is the field at $\mathbf{R}'$ due to the pseudo current:

$$\tilde{\mathbf{B}}_{ind}(\mathbf{R}') = \frac{1}{c} \int \left(\frac{e\hbar}{im_e} \sum_n^{occ} f_n \tilde{\psi}_n^*(\mathbf{r}) \nabla \tilde{\psi}_n(\mathbf{r}) \right.$$
$$\left. - \frac{e^2}{m_e c} \mathbf{A}_0(\mathbf{r}) \tilde{\rho}(\mathbf{r}) \right) \times \frac{(\mathbf{R}' - \mathbf{r})}{|\mathbf{R}' - \mathbf{r}|^3} \, d^3r$$
$$= \frac{1}{c} \int \tilde{\mathbf{j}}(\mathbf{r}) \times \frac{(\mathbf{R}' - \mathbf{r})}{|\mathbf{R}' - \mathbf{r}|^3} \, d^3r. \tag{35}$$

The one-center corrections are

$$\tilde{\mathbf{B}}^1_{ind}(\mathbf{R}') - \mathbf{B}^1_{ind}(\mathbf{R}') = \frac{1}{c} \sum_{\mathbf{R}} \sum_{ij} \bar{\rho}_{\mathbf{R}ij} \left(D^1_{ij} \left[\mathbf{j}^{in}_{\mathbf{R}}(\mathbf{r}) \times \frac{(\mathbf{R}' - \mathbf{r})}{|\mathbf{R}' - \mathbf{r}|^3} \right] \right.$$
$$\left. - \tilde{D}^1_{ij} \left[\mathbf{j}^{in}_{\mathbf{R}}(\mathbf{r}) \times \frac{(\mathbf{R}' - \mathbf{r})}{|\mathbf{R}' - \mathbf{r}|^3} \right] \right). \tag{36}$$

Note that the terms $\mathbf{R} \neq \mathbf{R}'$ have a multi-center character. These can be handled via an augmentation procedure (Sec. III A 3). The currents $\mathbf{j}^{in}_{\mathbf{R}}(\mathbf{r})$ have the gauge origin shifted to the center of the PAW spheres $[\mathbf{A}_0(\mathbf{r}) \rightarrow \mathbf{A}_0(\mathbf{r} - \mathbf{R})]$.

Now we discuss the "standard" route to $\mathbf{B}_{ind}(\mathbf{R}')$, i.e., the route via the current density. The GIPAW transform, Eq. (30), of the current operator yields three terms:

$$\tilde{\mathbf{J}}(\mathbf{r}) = \mathbf{J}(\mathbf{r}) + \sum_{\mathbf{R}} \left(\bar{\mathbf{J}}^1_{\mathbf{R}}(\mathbf{r}) - \tilde{\bar{\mathbf{J}}}^1_{\mathbf{R}}(\mathbf{r}) \right). \tag{37}$$

Here $\mathbf{J}$ is just the sum of the AE para and diamagnetic current operators, Eqs. (6) and (7). The first term on the right-hand side is the usual plane wave part, whereas the second and third terms are the all-electron and pseudo one-center terms, respectively.

For the plane wave part, the current operator is identical to the usual all-electron current operator. An important issue to address is that the vector potential, and hence the diamagnetic current, increases linearly with the distance from the gauge origin. In the complete basis set limit this increase is exactly compensated by the paramagnetic current, as is easily recognized by considering Eq. (28), and the action of the gradient operator in the paramagnetic current on the exponent. However, the further the atoms are located away from the gauge origin, the more the "local" effective plane wave cutoff is reduced at a specific site. Hence, the freedom in the basis set expansion (Eq. (27)) is locally reduced, and a higher global kinetic energy cutoff is needed. The familiar gauge problem now manifests itself in slower plane-wave basis set convergence. We did not attempt to correct for this effect,[29] since convergence in the plane wave basis, i.e., perfect cancellation over the molecule, is fairly easy to attain by increasing the plane wave cutoff (see Sec. IV).

For the one-center current terms the GIPAW transform yields

$$\bar{\mathbf{J}}^1_{\mathbf{R}}(\mathbf{r}) = \sum_{ij(\mathbf{R})} |\bar{\tilde{p}}_i\rangle D^1_{\mathbf{R}ij}[\mathbf{J}^{in}_{\mathbf{R}}(\mathbf{r})] \langle \bar{\tilde{p}}_j|$$
$$= \sum_{ij(\mathbf{R})} |\bar{\tilde{p}}_i\rangle \langle \phi_i| \mathbf{J}^{in}_{\mathbf{R}}(\mathbf{r}) |\phi_j\rangle \langle \bar{\tilde{p}}_j| \tag{38}$$

and an analogous term for the pseudo one-center current operator $\tilde{\bar{\mathbf{J}}}^1_{\mathbf{R}}(\mathbf{r})$. Here $D^1_{\mathbf{R}ij}[\mathbf{J}^{in}_{\mathbf{R}}(\mathbf{r})]$ is implicitly defined in the second line and the gauge twisted current operator in the one-center spheres is

$$\mathbf{J}^{in}_{\mathbf{R}}(\mathbf{r}) = \frac{e\hbar}{2im_e} (\nabla |\mathbf{r}\rangle \langle \mathbf{r}| + |\mathbf{r}\rangle \langle \mathbf{r}| \nabla) - \frac{e^2}{m_e c} \mathbf{A}_0(\mathbf{r} - \mathbf{R}) |\mathbf{r}\rangle \langle \mathbf{r}|. \tag{39}$$

As always, the gauge problem is eliminated by shifting the gauge origin to the center of the PAW sphere. Note that the $D^1_{\mathbf{R}ij}[\mathbf{J}^{in}_{\mathbf{R}}(\mathbf{r})]$ are functions of $\mathbf{r}$.

The Biot-Savart law (Eq. (15)) now provides the route from $\mathbf{j}$ to the induced field $\mathbf{B}_{ind}$ at a nucleus $\mathbf{R}'$. It consists of a contribution arising from the pseudo-current density and *multi-center* corrections:

$$\mathbf{B}_{ind}(\mathbf{R}') = \tilde{\mathbf{B}}_{ind}(\mathbf{R}') + \mathbf{B}^1_{ind}(\mathbf{R}'). \tag{40}$$

The first term on the right-hand side is

$$\tilde{\mathbf{B}}_{ind}(\mathbf{R}') = \frac{1}{c} \sum_n f_n \int \langle \tilde{\psi}_n| \mathbf{J} |\tilde{\psi}_n\rangle \times \frac{\mathbf{R}' - \mathbf{r}}{|\mathbf{R}' - \mathbf{r}|^3} \, d^3r,$$

where $\mathbf{J}$ is the total current, i.e., the sum of Eqs. (8) and (9). It is $\tilde{\mathbf{B}}_{ind}(\mathbf{R}')$ as obtained before in Eq. (35). The plane wave current density $\tilde{\mathbf{j}} = \sum_n f_n \langle \tilde{\psi}_n| \mathbf{J} |\tilde{\psi}_n\rangle$ is set up on the plane wave grid, and Biot-Savart is applied using a combination of fast and slow Fourier transforms (just as by YPM).[10] The multi-center corrections are

$$\mathbf{B}^1_{ind}(\mathbf{R}') = \frac{1}{c} \sum_{\mathbf{R}} \sum_{ij} \bar{\rho}_{\mathbf{R}ij} \int \left(D^1_{ij} \left[\mathbf{J}^{in}_{\mathbf{R}}(\mathbf{r}) \right] - \tilde{D}^1_{ij} \left[\mathbf{J}^{in}_{\mathbf{R}}(\mathbf{r}) \right] \right)$$
$$\times \frac{(\mathbf{R}' - \mathbf{r})}{|\mathbf{R}' - \mathbf{r}|^3} \, d^3r, \tag{41}$$

where the integrations are restricted to the PAW spheres, as the partial waves vanish outside. Although the expression seems to be somewhat different from Eq. (36), it actually is identical (the different notation is due to the GIPAW transform being done either on the expectation value of the Hamiltonian or on the current density). Expression (41) consists of two-center ($\mathbf{R} \neq \mathbf{R}'$) contributions and a single one-center ($\mathbf{R} = \mathbf{R}'$) contribution for each atom $\mathbf{R}'$. The latter is calculated numerically exact, expanding all contributions in radial functions times spherical harmonics, where the radial integrals are performed on logarithm radial meshes. Since the two-center terms are generally quite small, YPM neglect these contributions in their linear response method.[10] Below we describe a simple procedure wherein these terms are accurately approximated by pseudized augmentation contributions on the plane wave grid analogously to the charge augmentation in the PAW method. Numerical tests for this extra term are shown in Sec. IV, finding important corrections for the shielding of hydrogen atoms.

3. Current augmentation

The two-center contributions in Eq. (41) are conveniently handled via a multipole expansion. As the D_{ij}^1 are from other PAW spheres than $\mathbf{R}'$, the detailed current pattern inside the spheres does not matter, and only the moments of the current density determine the field at $\mathbf{R}'$. Hence, we can replace the rapidly varying currents $D_{ij}^1[\mathbf{J}_\mathbf{R}^{in}(\mathbf{r})]$ by a smooth current density, i.e., slowly varying in space, with equal moments, with the requirement that the "pseudo" current density can be accurately described on the plane wave grid. The corresponding field is once again obtained via the Biot-Savart law on the plane wave grid.

The implementation is analogous to the calculation of the compensation charge density,[27] and it is reminiscent of the current integration in the LAPW.[14] The moments of the difference between the all-electron current and the pseudo current are calculated as integrals over the PAW sphere:

$$\mathbf{I}_{ij\mathbf{R}}^{LM} = \int \left(D_{ij}^1[\mathbf{J}_\mathbf{R}^{in}(\mathbf{r})] - \tilde{D}_{ij}^1[\mathbf{J}_\mathbf{R}^{in}(\mathbf{r})] \right) |\mathbf{r}-\mathbf{R}|^L Y_{LM}(\mathbf{R}) \, r^2 \, dr \, d\Omega$$

(42)

and, for $\mathbf{R} \neq \mathbf{R}'$, the following replacement is made in Eq. (41):

$$D_{ij}^1[\mathbf{J}_\mathbf{R}^{in}(\mathbf{r})] - \tilde{D}_{ij}^1[\mathbf{J}_\mathbf{R}^{in}(\mathbf{r})] \rightarrow \sum_{LM} \mathbf{I}_{ij\mathbf{R}}^{LM} g_L(|\mathbf{r}-\mathbf{R}|) Y_{LM}(\mathbf{R}).$$

(43)

Here the g_L are smooth functions with moment 1. So the latter can be represented on the plane wave grid. It is multiplied with $\bar{\rho}_{\mathbf{R}ij}$ and added to the plane wave current density $\tilde{\mathbf{j}}$. In practice, we suppress the diamagnetic contribution to $\mathbf{J}_\mathbf{R}^{in}(\mathbf{r})$. The GIPAW has already made it vanish at $\mathbf{R}$, i.e., it is very weak.

B. Converse approach

Starting point is again the AE Hamiltonian, Eq. (12). Here $\mathbf{A}_s(\mathbf{r})$ is the vector potential of the external magnetic dipole $\mathbf{m}_s$ that is put at the nucleus $\mathbf{R}_s$ whereof we want to calculate the shielding. It is given by Eq. (11). $\mathbf{A}_0(\mathbf{r})$ is the vector potential of a uniform magnetic field according to Eq. (10). It is used to calculate the induced moment as magnetic field derivative, see Eq. (44) below.

We now derive the PAW Hamiltonian to be used in the self-consistent calculation and an expression for the response, i.e., the induced total magnetic moment. We closely follow CMLT,[18] but here extend to PAW with non-norm-conserving partial waves and restrict to a molecular picture. It is more natural to first discuss the response and next the Hamiltonian used for the self-consistent calculation.

1. Total induced moment

Using the Hellman-Feynman theorem, the total induced magnetization $\mathbf{M}_{ind}$ can be obtained as follows (cf. Eq. (20)):

$$\mathbf{m}_{ind} = -\left\langle \frac{\partial H}{\partial \mathbf{B}} \right\rangle = -\sum_n^{occ} f_n \langle \tilde{\psi}_n | \frac{\partial}{\partial \mathbf{B}} (\tilde{H} - \epsilon_n \tilde{S}) | \tilde{\psi}_n \rangle_{B=0}.$$

(44)

Here $\tilde{H}$ is the GIPAW transform of the AE Hamiltonian. To first order in $\mathbf{A}_s$ the AE Hamiltonian is:

$$H^{(0)} = \frac{1}{2m_e} \left(\mathbf{p} - \frac{e}{c} \mathbf{A}_{ind}(\mathbf{r}) \right)^2 + eV(\mathbf{r}),$$

$$H^{(1)} = -\frac{e}{2m_e c} (\mathbf{p} \cdot \mathbf{A}_s + \mathbf{A}_s \cdot \mathbf{p})$$

$$+ \frac{e^2}{2m_e c^2} (\mathbf{A}_{ind} \cdot \mathbf{A}_s + \mathbf{A}_s \cdot \mathbf{A}_{ind}).$$

In converting to the GIPAW Hamiltonian we only retain terms *linear in* $\mathbf{B}$. First we consider $H^{(0)}$. Its inner operator GIPAW transform yields a one-center contribution:

$$-\frac{e}{2m_e c} \mathbf{B} \cdot |\tilde{p}_{\mathbf{R}i}\rangle \left(D_{\mathbf{R}ij}^1[\mathbf{L_R}] - \tilde{D}_{\mathbf{R}ij}^1[\mathbf{L_R}] \right) \langle \tilde{p}_{\mathbf{R}j}|, \quad (45)$$

where $\mathbf{L_R} = (\mathbf{r} - \mathbf{R}) \times \mathbf{p}$ is the angular momentum operator centered on atom $\mathbf{R}$. It vanishes for PAW data sets with norm-conserving pseudo partial waves. The outer operator transform [of $V(\mathbf{r})$] yields an another one-center term linear in $\mathbf{B}$:

$$\frac{ie}{2\hbar c} \mathbf{B} \cdot (\mathbf{R} \times [\mathbf{r}, V_{nl}]) \text{ where}$$

$$V_{nl} = |\tilde{p}_{\mathbf{R}i}\rangle \left(D_{\mathbf{R}ij}^1[eV] - \tilde{D}_{\mathbf{R}ij}^1[eV] \right) \langle \tilde{p}_{\mathbf{R}j}|.$$

(46)

Here the strength parameters are understood to include also the usual one-center contribution to the kinetic energy. Transforming the second term ($H^{(1)}$) yields the one-center contribution:

$$\frac{e^2}{2m_e c^2} \mathbf{B} \cdot |\tilde{p}_{\mathbf{R}i}\rangle \left(D_{\mathbf{R}ij}^1[(\mathbf{r} - \mathbf{R}) \times \mathbf{A}_s] \right.$$

$$\left. - \tilde{D}_{\mathbf{R}ij}^1[(\mathbf{r} - \mathbf{R}) \times \mathbf{A}_s] \right) \langle \tilde{p}_{\mathbf{R}j}|. \quad (47)$$

This is the diamagnetic term of CMLT ($\mathbf{E}_\mathbf{R}^{NL}$, their Eq. (17)).[18] The first term of $H^{(1)}$, which is independent of $\mathbf{B}$, only yields a linear contribution via the outer transform:

$$\frac{ie}{2\hbar c} \mathbf{B} \cdot (\mathbf{R} \times [\mathbf{r}, K_{nl}]) \text{ with}$$

$$K_{nl} = -\frac{e}{2m_e c} |\tilde{p}_{i\mathbf{R}}\rangle \left(D_{\mathbf{R}ij}^1[\mathbf{p} \cdot \mathbf{A}_s + \mathbf{A}_s \cdot \mathbf{p}] \right. \quad (48)$$

$$\left. - \tilde{D}_{\mathbf{R}ij}^1[\mathbf{p} \cdot \mathbf{A}_s + \mathbf{A}_s \cdot \mathbf{p}] \right) \langle \tilde{p}_{j\mathbf{R}}|.$$

Transforming the overlap operator gives a result similar to the above with S_{nl} instead of K_{nl}:

$$S_{nl} = |\tilde{p}_{i\mathbf{R}}\rangle Q_{\mathbf{R}ij} \langle \tilde{p}_{j\mathbf{R}}|. \quad (49)$$

We now add the one-center contributions (45)–(49) to the AE Hamiltonian (to linear order in $\mathbf{B}$, Eq. (13)). The result, $\tilde{H} - \epsilon_n \tilde{S}$ is substituted in Eq. (44), giving the total induced magnetic moment $\mathbf{m}_{ind}$:

$$\mathbf{m}_{ind} = \Omega_c \mathbf{M}_{ind} = \tilde{\mathbf{m}}_{ind} + \mathbf{m}_L^1 + \mathbf{m}_{dia}^1 + \mathbf{m}_{NL}^1.$$

Here $\tilde{\mathbf{M}}_{ind}$ is the plane wave contribution, i.e., the magnetic moment of the current with a field $\mathbf{A}_s$ according to Eq. (19):

$$\tilde{\mathbf{m}}_{ind} = \frac{1}{2c} \int \mathbf{r} \times \left(\frac{e}{m_e} \sum_n f_n \text{Im}[\psi_n^* \nabla \psi_n] - \frac{e^2}{m_e c} \mathbf{A}_s(\mathbf{r}) \tilde{\rho}(\mathbf{r}) \right) d^3r. \quad (50)$$

The one-center contributions are:

$$\mathbf{m}_L^1 = \frac{e}{2m_e c} \sum_{ij\mathbf{R}} \rho_{ij\mathbf{R}} \left(D_{\mathbf{R}ij}^1[\mathbf{L_R}] - \tilde{D}_{\mathbf{R}ij}^1[\mathbf{L_R}] \right),$$

$$\mathbf{m}_{\text{dia}}^1 = -\frac{e^2}{2m_e c^2} \sum_{ij\mathbf{R}} \rho_{ij\mathbf{R}}$$

$$\left(D_{\mathbf{R}ij}^1[(\mathbf{r} - \mathbf{R}) \times \mathbf{A}_s] - \tilde{D}_{\mathbf{R}ij}^1[(\mathbf{r} - \mathbf{R}) \times \mathbf{A}_s] \right),$$

$$\mathbf{m}_{\text{NL}}^1 = -\frac{ie}{\hbar c} \sum_n f_n \sum_{\mathbf{R}} \mathbf{R} \times \langle \tilde{\psi}_n | [\mathbf{r}, V_{\text{nl}} + K_{\text{nl}} - \epsilon_n S_{\text{nl}}] | \tilde{\psi}_n \rangle.$$

Comparing to the magnetization expressions of CMLT, we observe that $\mathbf{m}_L^1$ and the overlap contribution to $\mathbf{m}_{\text{NL}}^1$ are absent in their method, as these vanish for norm-conserving PAW data sets. Our $\mathbf{m}_{\text{dia}}^1$ corresponds to their $\mathbf{M}_{\text{dia}}$. The V_{nl} and K_{nl} parts of $\mathbf{m}_{\text{NL}}^1$ correspond to the long range part of their $\mathbf{M}_{\text{NL}}$ and $\mathbf{M}_{\text{para}}$, respectively (Eqs. (22) and (25) of Ref. 18).

2. PAW Hamiltonian

The starting point is again the Hamiltonian for zero magnetic field, Eq. (33). We again consider the first-order changes upon switching on the external dipole moment $\mathbf{m}_s$ at $\mathbf{R}_s$, but now in vanishing magnetic field, i.e., the GIPAW becomes regular PAW:

$$H^{\text{PAW,s}} = H^{\text{PAW}} - \frac{e}{m_c c}\mathbf{A}_s \cdot \mathbf{p}$$

$$- \frac{e}{2m_e c} \sum_{ij\mathbf{R}} \rho_{ij\mathbf{R}} \left(D_{\mathbf{R}ij}^1[\mathbf{A}_s \cdot \mathbf{p} + \mathbf{p} \cdot \mathbf{A}_s] \right.$$

$$\left. - \tilde{D}_{\mathbf{R}ij}^1[\mathbf{A}_s \cdot \mathbf{p} + \mathbf{p} \cdot \mathbf{A}_s] \right). \quad (51)$$

The vector potential on the plane wave grid is conveniently set up in reciprocal space. The one-center terms split into two kinds: (a) There is one contribution to the sum with $\mathbf{R} = \mathbf{R}_s$. This term is calculated numerically exact, by expanding the term in products of spherical harmonics and radial functions, and performing the radial integration on the logarithmic PAW one-center grid. (b) The other terms, i.e., where $\mathbf{R} \neq \mathbf{R}_s$, are usually small and typically neglected. However, analogous to the "current augmentation" described above (Sec. III A 3), they can also be included in an augmentation procedure on the plane wave grid. This is described below.

3. Completing the Hamiltonian: D_{ij} augmentation

The $D_{\mathbf{R}ij}^1$ in Eq. (51) can be calculated using the expansion of the paramagnetic current operator in Eq. (43) from Sec. III A 3. We rewrite the one-center strength parameters using:

$$\langle \phi_i | \mathbf{A}_s \cdot \mathbf{p} | \phi_j \rangle = \frac{\hbar}{i} \int d^3r \ \langle \phi_i | \mathbf{A}_s \cdot | \mathbf{r} \rangle \langle \mathbf{r} | \nabla | \phi_j \rangle$$

$$= \frac{\hbar}{i} \int d^3r \ \mathbf{A}_s(\mathbf{r}) \cdot \langle \phi_i | \mathbf{r} \rangle \langle \mathbf{r} | \nabla | \phi_j \rangle.$$

In fact, the strength parameters are proportional to the integral over the PAW spheres of the product of $\mathbf{A}_s$ and the paramagnetic current density. We approximate the latter using the expansion in Eq. (43), since $\mathbf{A}_s$ is slowly varying except for the sphere $\mathbf{R} = \mathbf{R}_s$, where the integral is done numerically as described in Sec. III B 2. Since the current augmentation restores the moments of the all-electron current density exactly, and source terms are absent except at $\mathbf{R} = \mathbf{R}_s$, the described procedure allows for an exact evaluation of two center terms in $\langle \phi_i | \mathbf{A}_s \cdot \mathbf{p} | \phi_j \rangle$.

IV. NUMERICAL CONSIDERATIONS AND TESTS

Below we provide general computational details, discuss basis set, box size convergence, required accuracy of the Kohn-Sham (KS) orbitals, linearity of the response, assess the importance of two-center terms (Eqs. (34) and (51)), and validate the implementation for several molecules. For the latter we compare to results obtained with various linear-response implementations. Finally, we briefly discuss computational performance.

A. General computational details

To obtain all 9 independent components of the shielding tensor in general three calculations are needed, one for each Cartesian direction of the external perturbation in Eq. (16) or (21). In the direct approach one thus obtains the shielding tensors for all nuclei. In the converse approach this yields the tensor for one selected nucleus, so calculations need to be repeated for each nucleus considered.

NMR experiments do not provide direct access to all 9 components of the shielding tensor. To obtain the NMR observables one first has to symmetrize the tensor and bring it to principal axes by diagonalization. Following Mason (Ref. 30) the isotropic absolute shielding σ_{iso}, the span Ω and the skew κ are obtained as

$$\sigma_{iso} = \frac{1}{3}(\sigma_{11} + \sigma_{22} + \sigma_{33}),$$

$$\Omega = \sigma_{33} - \sigma_{11}, \quad (52)$$

$$\kappa = \frac{3(\sigma_{22} - \sigma_{iso})}{\Omega},$$

where the three principal components σ_{ii} are ordered such that

$$\sigma_{11} \leq \sigma_{22} \leq \sigma_{33}. \quad (53)$$

This is one of the frequently used definitions of the Chemical Shielding Anisotropy (CSA) tensor. σ_{iso}, Ω, and κ can be obtained from experimental spectra in principle.

Below we only report the valence contribution to the shielding. In the Coulomb gauge the core contribution is independent of the chemical environment.[6] Wherever we compare to all-electron results obtained with DALTON the core shielding has been subtracted.[31]

In all calculations the GGA-PBE (Generalized Gradient Approximation-Perdew-Burke-Ernzerhof) DFT functional was used,[32,33] with consistently build PAW data sets. Table I lists a brief compilation of the most important parameters.

TABLE I. Parameters of the PAW data sets used. r_c^ℓ are the cutoff radii for the partial waves.

		r_c^ℓ (a.u.)		
	Frozen core	$\ell = 0$	$\ell = 1$	$\ell = 2$
H		1.1	1.1	
H_GW		0.95	1.1	1.1
C, C_GW	$1s^2$	1.2	1.5	
O, O_GW	$1s^2$	1.2	1.52	
O_h_GW	$1s^2$	1.0	1.1	1.1
N, N_GW	$1s^2$	1.3	1.5	
N_h	$1s^2$	1.1	1.1	
F_GW	$1s^2$	1.1	1.4	
P	$1s^2 2s^2 2p^6$	1.9	1.9	
P_d	$1s^2 2s^2 2p^6$	1.9	1.9	1.9

B. Convergence issues

Here we focus on the main parameters controlling the accuracy of the chemical shielding tensor. Following CMLT we use a water molecule as illustration.[34] PAW data sets practically identical to the standard data sets provided with VASP were used (named: H_GW, O_GW);[35] as already emphasized these potentials are not norm-conserving and require charge augmentation on the plane wave grid. Both the H and the O data set have 2 augmentation channels for $\ell = 0$ and $\ell = 1$. The H data set has a single $\ell = 2$ augmentation channel whereas for O the $\ell = 2$ channel provides the local pseudopotential.

The accuracy of the calculated shieldings is not only determined by the size of the plane-wave basis set (via the cutoff energy E_{cut}), but also by the quality of the PAW data set. To test this aspect we carried out some calculations with a (non-standard) harder O data set (see "O_h_GW" in Table I), constructed with smaller core radii and $\ell = 3$ local pseudopotential (unless explicitly stated, the standard O data set was used).

The data sets were not optimized for shielding calculations.

1. Plane wave basis set and super-cell convergence

Figure 2 shows how the ^{1}H isotropic shielding depends on the cutoff energy E_{cut} on the plane wave basis set, the molecular position t in the super-cell and the super-cell size L (cf. Fig. 3). For the direct approach, the dependencies on E_{cut} and molecular position t are related. Below we first discuss the direct approach, and next compare to the converse approach.

In the direct approach the saw-tooth vector potential makes a "jump" half-way the cell. To obtain meaningful shieldings, the Kohn-Sham orbitals should have vanishingly small amplitude in that region. This is illustrated in Fig. 2(a). It shows how the shielding for one of the H nuclei in the H$_2$O molecule changes when it is translated along one of the edges of the cell. Near $t = 0$ and $t = L$ we observe a plateau. Here we obtain a meaningful number for the shielding. In the region halfway the cell the orbitals sense the jump in the vector
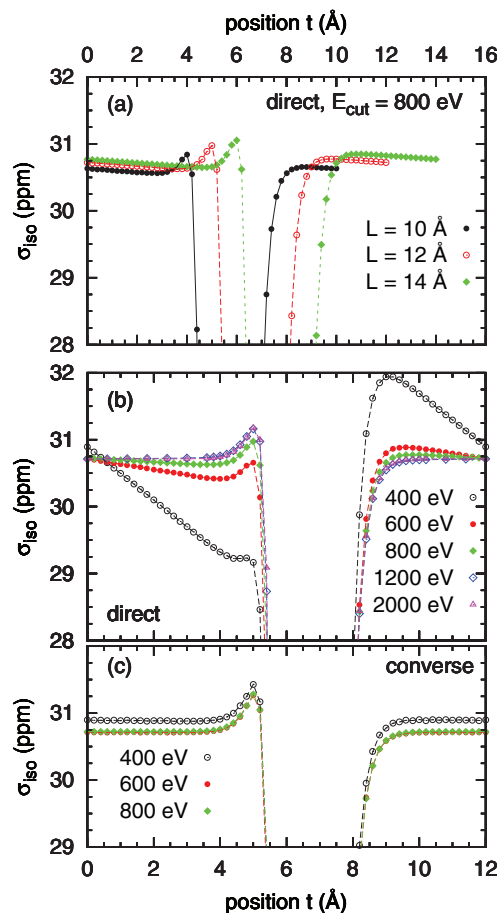

FIG. 2. Convergence properties of the direct approach illustrated with ^{1}H isotropic chemical shielding of a H$_2$O molecule. (a) Shieldings as a function of molecular position (t is the distance of the H nucleus from the origin) for supercells of various sizes L using the direct approach. The molecule is translated along the (x) edge of the supercell. (b) and (c) Shieldings for a fixed length cell ($L = 12$ Å) as a function of kinetic energy cutoff for the direct (b) and converse (c) approach.
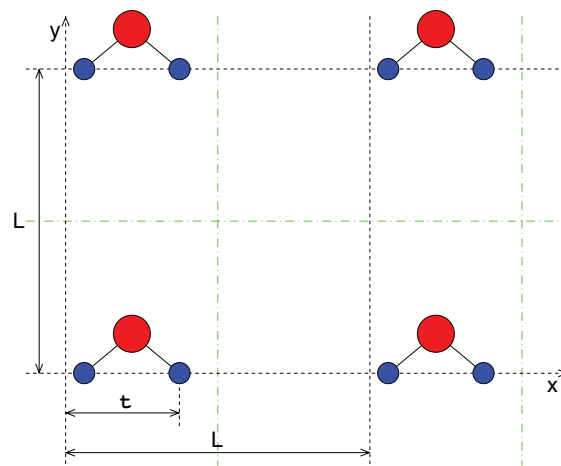

FIG. 3. Position of the H$_2$O molecule in the unit cell. It lies in the xy-plane. The right-hand-side H nucleus is at distance t from the corner of the unit cell (the gauge origin). Unit cell boundaries are indicated with a black dashed line. The applied vector potential makes a jump half-way the unit cell at $L/2$ (dashed-dotted green lines).

potential and large deviations from the correct shielding occur. The plateau region, where the correct shielding is obtained, increases linearly with the cell size L.

The plateau in Fig. 2(a) has a small inclination. This is due to the gauge problem described in Sec. III A 2. It is better illustrated in Fig. 2(b) that shows the cutoff dependence of the shielding for the molecule that is dragged along the edge of the cell. The further the H nucleus is from the gauge origin at $t = 0$, the larger the deviation from the true value. For a kinetic energy cutoff of 400 eV the variation of σ_{iso} across the inclined plateau is about 3 ppm, and the error can be as large as 2 ppm. Increasing the cutoff reduces the inclination. For an 800 eV cutoff the maximum error is less than 0.1 ppm, which is sufficiently accurate for practical purposes, even for H shieldings. For 1200 eV it is of the order of $\sim$0.02 ppm. As the error is linear in the distance, large molecules might require a slightly larger cutoff. In practice good accuracy is easily attained (see the illustration below, Sec. IV E).

In the converse method the need for a discontinuous vector potential does not emerge, however, Fig. 2(c) shows that half-way the cell meaningless results are obtained. This is an artifact of the moment calculation: the range of $\mathbf{r}$ in the calculation of the plane-wave moment $\tilde{\mathbf{m}}_{ind}$ in Eq. (50) is from $-L/2$ to $L/2$ (a similar restriction applies to $\mathbf{R}$ in the calculation of $\mathbf{M}_{NL}^1$) so meaningless results are obtained if the molecule crosses the "boundary" at $L/2$. Further we note that the plateaus do not exhibit any inclination. This is because a gauge problem has been avoided by choosing *the origin for the moment calculation always at the nucleus were* $\mathbf{m}_s$ *is placed*.

Figure 4 shows the convergence of the isotropic shielding with increasing plane wave kinetic energy cutoff E_{cut}, with the relevant nucleus placed at the gauge origin. *Both methods*

TABLE II. Oxygen and hydrogen isotropic chemical shielding calculated with various PAW data sets. Shieldings are extrapolated to infinite cell size and converged in plane wave basis set ($E_{cut} = 2000$ eV). DALTON calculations in vacuum are with an aug-cc-pCV5Z basis set.

		Converse		Direct	
	Augm.	$\sigma(^1\mathrm{H})$	$\sigma(^{17}\mathrm{O})$	$\sigma(^1\mathrm{H})$	$\sigma(^{17}\mathrm{O})$
Standard O	No	30.84	49.49	30.84	49.49
Standard O	Yes	30.34	49.60	30.34	49.60
Hard O	No	31.33	50.37	31.33	50.37
Hard O	Yes	30.71	50.48	30.71	50.48
DALTON		30.76	50.58	30.76	50.58

yield identical shieldings, and also exhibit a similar convergence behavior. Only for low cutoff small differences occur. With standard PAW data sets very good convergence is attained for $E_{cut} = 800$ eV. For this cutoff the plane-wave gauge problem is only marginal (see above). For practical purposes even a cutoff of 600 eV would be sufficient. This cutoff is somewhat larger than typically needed for calculation of total energies, forces, etc.

Figure 4 also shows the plane-wave convergence with the harder O data set (same data set for H as before). Evidently convergence is much slower. For oxygen reasonable (not full) convergence is attained at $E_{cut} = 800$ eV. Hydrogen shieldings are well-converged for $E_{cut} = 900$ eV. The figure also shows that the harder O PAW data set yields different (plane-wave) converged shieldings. Table II compares the converged shieldings to accurate AE numbers. Depending on whether two-center corrections are applied (see Sec. IV C for a discussion), and on the PAW data set quality, hydrogen (oxygen) shieldings vary over a range of 0.5 (1) ppm. Without two-center augmentation corrections and using a standard O PAW data set, the hydrogen shielding agrees very well with the AE number (from DALTON). This nice agreement is fortuitous, as two-center corrections decrease the shielding by 0.5 ppm. Indeed, only with a hard oxygen data set and with two-center corrections applied, both the H and O shieldings are within 0.1 ppm of the AE numbers.

Another aspect of our supercell approach is the spurious interaction with periodic images. It is apparent in Fig. 2(a) where the inclined plateaus do not exactly coincide for different cell sizes. This error is typically small, and arises for any periodic method. There is no direct chemical interaction between the molecule and its periodic images. The magnetic field arising from the induced currents in the periodic images is felt, however. In leading order it is a dipolar field (or higher, depending on the molecular geometry and the position of the nucleus in the molecule). So we expect a scaling of the spurious contributions to σ_{ij} with $1/L^3$ (or higher). This is illustrated in Fig. 5, where $\sigma_{iso}(\mathrm{H})$ is plotted against $1/L^3$. For $L > 10$ Å a perfect scaling is observed. The line is a linear extrapolation from only the $L = 10$ and $L = 12$ Å results. So it is easy to correct for errors arising from the induced currents in the periodic images. However, often such errors are small. In the following we typically use cells of 16 Å edge length ($1/L^3 = 2.4 \times 10^{-4}$ Å^{-3}) and neglect remaining errors.
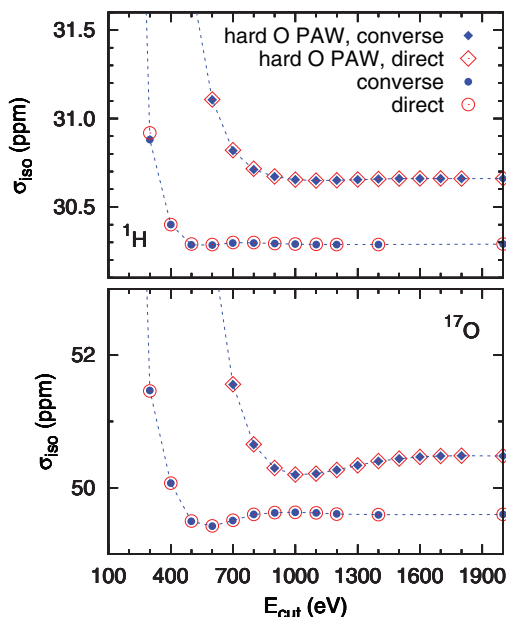

FIG. 4. Convergence of the hydrogen (top) and oxygen (bottom) chemical shielding of a water molecule as a function of the kinetic energy cut-off. For the direct approach the H (O) shielding has been calculated with the H (O) nucleus at the gauge origin. $L = 16$ Å.
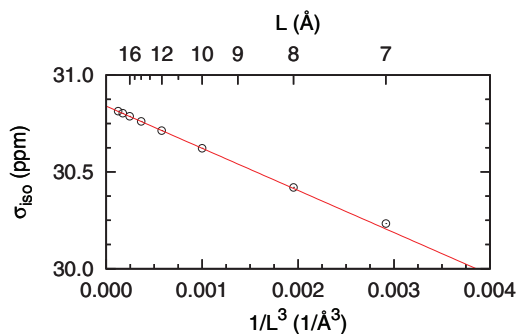
FIG. 5. ^{1}H isotropic chemical shielding of a H_2O molecule as a function of inverse supercell volume using the direct method. The molecular position is fixed and the kinetic energy cutoff $E_{cut} = 2000$ eV. L is the supercell size.

Table III shows the dependence on super cell size. Again we see that *both methods yield identical shieldings*, for box sizes sufficiently large that chemical interactions with the images are absent. Application of a periodic array of moments (in the converse approach) has the same effect as putting images of the molecule on the same array in a finite uniform field (in the direct approach). Also note that the spurious (dipolar) field from the periodic images is not uniform throughout the molecule.

2. The linear regime and orbital convergence

Both methods use a finite-field approach. To ensure reliable calculated shieldings the response fields should depend linearly on the applied perturbations. In order to establish the linear regime for both methods we performed calculations for a wide range of the strengths of the external field. Figure 6 shows an overview of these tests for the two sites of our water test molecule. We plot the difference between the isotropic shielding for a given perturbation and a fixed reference value while the strength of the perturbation is varied. The linear regime is indicated by the plateau (at zero). For both approaches the linear regime extends over many decades.

The perturbations applied are typically very small. So a very good convergence of the KS orbitals is mandatory. Here we pressed convergence to the limit. So the lower bound on the linear regime is set by inaccuracies of the code, the upper bound by nonlinearity of the response.

TABLE III. Convergence of oxygen and hydrogen shielding in a water molecule for the direct and the converse approach as a function of the size L of the cubic supercell. $E_{cut} = 1000$ eV.

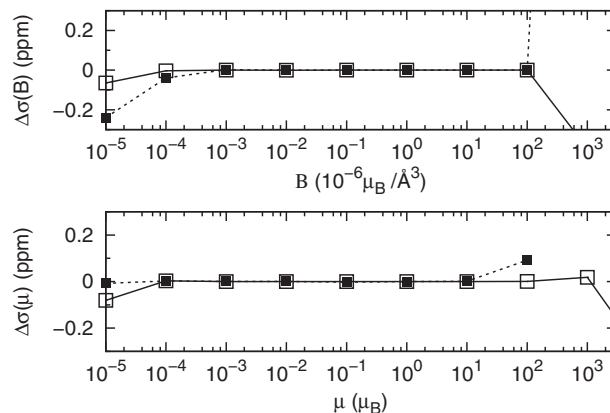| L (Å)	Converse		Direct	
	$\sigma(^1H)$	$\sigma(^{17}O)$	$\sigma(^1H)$	$\sigma(^{17}O)$
8	30.40	49.04	30.42	49.11
12	30.71	49.51	30.71	49.51
16	30.79	49.53	30.78	49.53
20	30.81	49.53	30.81	49.53
24	30.82	49.53	30.82	49.53
DALTON	30.76	50.58	30.76	50.58

FIG. 6. Dependence of the calculated chemical shift on the strength of the external field for the two sites of a water molecule: (top) By the direct approach and (bottom) by the converse approach. All calculations are PBE. $E_{cut} = 1000$ eV, $L = 16$ Å.

In practice one should choose the size of the perturbation as large as possible, but the response should still be linear. Thus the number of required iterations is minimized. Often it is most efficient to start from a well-converged solution that was obtained without any perturbation applied. No self-consistency in the perturbation is needed, so one just takes the fixed Kohn-Sham potential and applies the external moment or field. One should not restart from KS orbitals obtained with a different direction of the external perturbation as that gives slow convergence. Typically convergence for the converse approach is a bit faster.

C. Two-center contributions

Two-center contributions to the shieldings were not included in previous implementations of GIPAW chemical shielding.[10, 18] Here, we explore the effect of two-center contributions using the augmentation schemes of Secs. III A 3 and III B 3. We confirm that the two-center contributions yield only small corrections to the shielding. For nuclei with a large chemical shielding range these can safely be neglected. For hydrogen, its nucleus having a small shielding range (~20 ppm), two-center corrections do matter. They remove most remaining discrepancies between GIPAW and all-electron shieldings. We already saw this illustrated for the H_2O molecule in Table II.

Table IV presents hydrogen chemical shieldings of various small molecules containing carbon, nitrogen, or phosphorous. We list isotropic shieldings calculated with the two finite-field methods, both without and with augmentation contributions (current and D_{ij}-augmentation for direct and converse, respectively), and calculated using DALTON. For both methods the augmentation corrections are nearly identical. In some cases, they significantly contribute to the hydrogen chemical shielding. For example, for C_2H_2, the non-augmented result is $\sigma_{iso} = 28.43$ ppm whereas DALTON yields 30.39 ppm. Adding the augmentation contribution gives $\sigma_{iso} = 30.41$ ppm, nearly equal to the DALTON number. A similar improvement of almost 2 ppm is observed for N_2H_2. Both molecules have a triple C–C bond. For the other

TABLE IV. Hydrogen shieldings of various small molecules obtained by the direct and the converse approach with ("Yes") and without ("No") augmentation currents. Also shown: shieldings calculated in linear response with DALTON and VASP (VASP LR). Cubic supercells with 16 (14) Å edge length were used for the VASP finite field (linear response) calculations. Standard PAW data sets as supplied with VASP were used (for N the "N_h" data set was used, see Table I).

| Aug. | VASP finite field | | | | DALTON[a] | VASP LR |
| | Direct | | Converse | | | No |
	No	Yes	No	Yes		
CH$_4$	31.03	31.06	31.02	31.05	31.19	31.03
C$_2$H$_2$	28.43	30.41	28.43	30.41	30.39	28.43
C$_2$H$_4$	24.90	25.07	24.90	25.07	25.20	24.90
C$_2$H$_6$	30.17	30.17	30.17	30.17	30.36	30.17
C$_6$H$_6$[b]	23.36	23.46	23.36	23.47	23.66	23.33
N$_2$H$_2$	11.69	13.44	11.69	13.44	13.69	11.69
NH$_3$	31.33	31.14	31.33	31.14	31.27	31.33
P (std)						
PH$_3$	29.67	29.69	29.67	29.68	29.31	29.62
P_d						
PH$_3$	29.66	29.25	29.67	29.25	29.31	29.62
P$_2$H$_4$(1)[c]	29.00	28.60	29.00	28.61	28.79	29.00
P$_2$H$_4$(2)[c]	27.97	27.58	27.97	27.58	27.78	27.97

[a]aug-cc-pCV5Z but aug-cc-pCVQZ for phosphorous.
[b]18 Å box for finite field and 17 Å box for VASP LR.
[c]All VASP calculations with 14 Å box.

hydrocarbons and NH$_3$ the two-center effects are smaller. Hydrocarbons with only single bonds have negligible two-center corrections, those with double and aromatic bonds exhibit small corrections ($\sim$0.2 ppm).

For the systems containing phosphorous we used two different PAW data sets. The less accurate, standard P data set shows hardly any two-center corrections. The P_d data set is more accurate: it has explicit d-channel orbital reconstruction ($r_c = 1.9$ a.u. for all channels, the f-channel is the local pseudopotential). For the latter the two-center corrections are small but noticeable ($\sim$0.4 ppm). Evidently, the augmentation correction derives from the d-channel. Indeed, also core radii and augmentation charge densities affect such corrections.

Table V shows the impact of the augmentation correction on Ω and κ for the hydrocarbons. Augmentation improves the agreement with the DALTON numbers for most molecules. We attribute remaining discrepancies to the in-completeness of

TABLE V. Hydrogen anisotropic parameters Ω and κ of different hydrocarbon molecules obtained by the direct approach with and without augmentation current compared to DALTON results. All calculations are GGA-PBE.

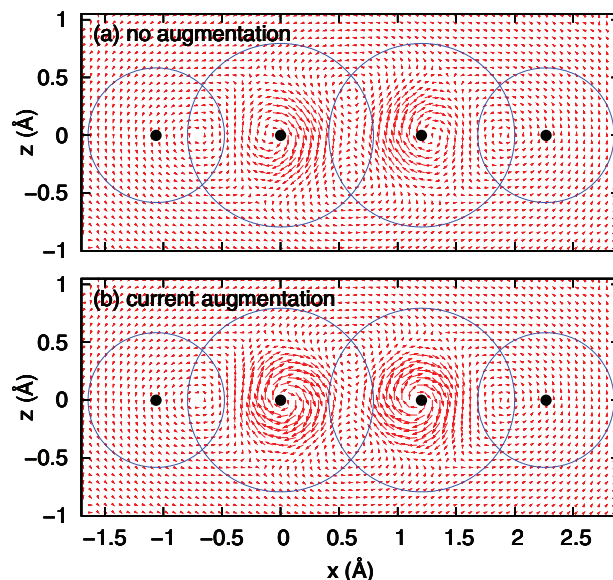| | VASP direct, finite field | | | | | |
| | No aug. | | Current aug. | | DALTON[a] | |
	Ω	κ	Ω	κ	Ω	κ
CH$_4$	9.06	1.000	8.60	1.000	9.21	1.000
C$_2$H$_2$	17.48	1.000	14.52	1.000	15.49	1.000
C$_2$H$_4$	7.10	-0.114	5.80	-0.129	5.62	-0.035
C$_2$H$_6$	10.47	0.385	10.10	0.394	10.69	0.416

[a]Linear response, aug-cc-pCV5Z.

FIG. 7. Induced pseudo current density in a C$_2$H$_2$ molecule calculated with the direct method. The molecule is on the x-axis. The applied field is in the positive y direction. The current density is represented by arrows on the plane-wave grid in the xz plane. Pseudo-current (a) without and (b) with current augmentation. Circles represent the PAW sphere radii, which are 1.5 a.u. and 1.1 a.u. for carbon and hydrogen, respectively.

the projectors in the PAW methods but cannot entirely exclude issues with the Gaussian basis sets, too.

Finally, we return to the C$_2$H$_2$ system, where the augmentation corrections are large. Figure 7 shows current density plots obtained with the direct method for this extreme case. The top (lower) panel shows the total pseudo-current without (with) the augmentation. The bare plane wave (i.e., without augmentation) current pattern shows strong currents in the region of the triple bond, but not at C–H bonds. The augmentation currents show an inverted picture, with strong currents in the region of the C–H bonds and weak currents in the region in-between the carbon atoms. The sum, shown in the lower panel, then exhibits neat circular currents going round both carbon nuclei. So both the yy and zz components of the shielding (in the axes of the figure) are strongly affected. The xx component is not affected.

D. Small molecules

In this section, we present a validation of the implementation of the two finite-field GIPAW approaches using small molecules. We present only calculations on phosphorous-containing molecules,[36] as the shielding of this nucleus is known to be poorly (insufficiently) reproduced in a pseudopotential plane-wave approach, i.e., a GIPAW reconstruction of the KS orbitals is known to be crucial.[7,10] Indeed, for light elements a pseudo-potential-only approach can give satisfactory results.[4]

In Table VI, the results of both finite-field approaches are compared to shieldings obtained with LR methods as implemented in the plane wave codes (i) VASP and (ii) QUANTUM-ESPRESSO, and (iii) in the all-electron code DALTON. Both (i) and (ii) are crystal methods, according to Refs. 10 and 7,

TABLE VI. Absolute isotropic phosphorous chemical shifts for several molecules calculated with the two finite-field (FF) approaches. Linear-response (LR) results obtained with VASP, QUANTUM-ESPRESSO(QE) and DALTON are presented for comparison. All calculations are GGA-PBE. A P_d data set was used for VASP ($E_{cut} = 1000$ eV). No PAW D_{ij} and current augmentation were applied. The core contribution of 908.9 ppm has been removed from QUANTUM-ESPRESSO and DALTON results.

	VASP FF		VASP	QE[a]	DALTON[b]
	Converse	Direct	LR	LR	LR
P_4	43.34	43.40	43.58	47.74	47.33
PH_3	331.29	331.29	331.34	331.43	332.15
P_2H_4	389.28	389.28	389.34	389.22	388.56
H_3PO_4	627.90	628.10	627.98	623.17	623.71
PF_3	758.13	758.13	758.16	750.88	753.08
P_2	1225.77	1225.77	1225.61	1227.52	1210.26
MAE[c]	5.05	5.08	5.01	3.63	0.0

[a] 100 Ry, cubic box of 16 Å, NC GIPAW potential.
[b] aug-cc-pCVQZ.
[c] Mean absolute error compared to DALTON.

respectively. Again, both finite-field approaches yield almost identical numbers that are also very similar to the VASP linear response results. Indeed, all those results have been obtained with identical PAW data sets (except the QE results). On average VASP and QE do an equally good job in reproducing the all-electron DALTON shieldings. VASP and QE results are somewhat different, showing the dependence on the PAW data sets (standard, non-norm-conserving P_d data set for VASP, and a norm-conserving data set for QE).

We would like to emphasize the fact that whereas the two finite-field approaches give identical results for the total shielding, they exhibit a very different behavior if one considers the various contributions to the shielding tensor. Table VII shows the partitioning into the two main contributions: the plane-wave (PW) and the one-center contributions. In the direct approach, the main contribution is given by the one-center terms. This is consistent with previous findings by Pickard and Mauri.[7] However, for the converse approach the behavior is radically different: the main contribution is given

TABLE VII. Partitioning of phosphorous chemical shifts into plane-wave (PW) and one-center terms for the finite-field (FF) direct and converse approach. All calculations are GGA-PBE.

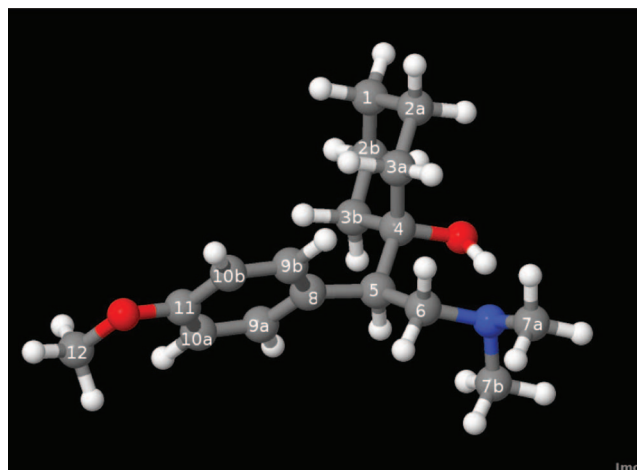| Molecule	PW	One-center	Total
	FF Converse (VASP)		
P_4	38.73	4.60	43.33
PH_3	402.46	-71.17	331.29
P_2H_4	455.82	-66.54	389.28
H_3PO_4	566.15	61.75	627.90
PF_3	710.92	47.22	758.13
P_2	1289.62	-63.85	1225.77
	FF Direct (VASP)		
P_4	-62.97	106.37	43.40
PH_3	-27.28	358.56	331.29
P_2H_4	-20.08	409.36	389.28
H_3PO_4	31.99	596.10	628.10
PF_3	31.33	726.81	758.13
P_2	46.39	1179.38	1225.77

FIG. 8. Venlafaxine molecule, containing oxygen (red), carbon (grey), nitrogen (blue), and hydrogen (white) atoms. Saturated ring: 1-2a-3a-4-3b-2b-1 and aromatic ring: 8-9a-10a-11-10b-9b-8. Figure made with Jmol.[38]

by the plane-wave term. Indeed, for a rough indication of the shielding one can neglect the one-center contributions.

E. Large molecules: Venlafaxine

Here we illustrate the feasibility of the approach for a relatively large molecule. We use a single venlafaxine (free base) molecule, $C_{17}O_2NH_{27}$. We study the gas phase shieldings, with the molecule frozen in its crystal conformation.[37] It contains a six-membered aromatic carbon ring, a saturated carbon ring, and several smaller groups (Fig. 8). It is put into a repeated cubic box of $15 \times 15 \times 15$ Å^3. Thus the periodic images are separated by vacuum regions of at least 5.7 Å in all three directions.

We calculate the shieldings using the direct and converse approaches without and with augmentation (current and D_{ij}-augmentation, respectively). For reference we compare with linear response calculations using the (crystal) GIPAW method of YPM (Ref. 10) with both VASP and QUANTUM-ESPRESSO, and the molecular GIAO linear response of DALTON. In our VASP calculations we used standard PAW data sets, as supplied with the package (data sets named: O, H, N, C). For QUANTUM-ESPRESSO we used norm-conserving data sets. All VASP calculations employed a kinetic energy cutoff of 900 eV. In the direct and converse molecular finite-field calculations we used Γ-point sampling only.

Figure 9 summarizes the main results. Panels [(a) and (b), (d) and (e)] show that both molecular approaches yield results that are identical to the YPM linear response (VASP implementation). This demonstrates the internal consistency of the VASP results. We also find very good agreement with the QUANTUM-ESPRESSO results [panels (c) and (f)]. There are some small differences that we attribute to differences in the PAW data sets.

The effect of current and D_{ij}-augmentation is quite small. For C, N, and O it can be safely neglected (not shown). For H the effect is also small, but as its shift has a very small range, it can be important nevertheless (see above). Panels (d)
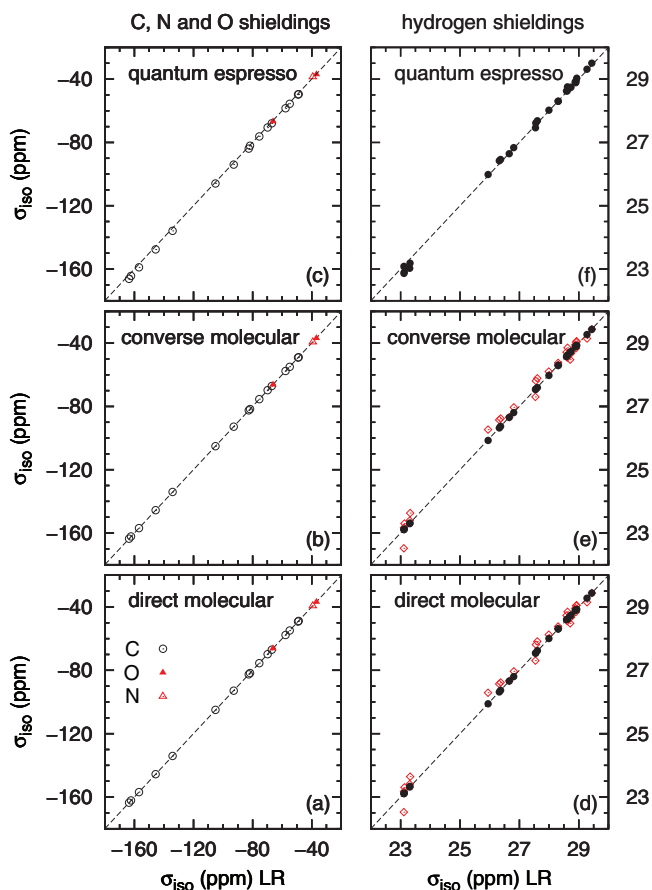
FIG. 9. Calculated shieldings for the venlafaxine free base molecule. Abscissa: isotropic shieldings calculated with linear response (LR) and VASP (no augmentation corrections). Ordinate: isotropic shieldings calculated with the direct molecular method [(a) and (d)], with the converse molecular methods [(b) and (e)] and with QUANTUM-ESPRESSO using linear response [(c) and (f)]. Hydrogen shieldings calculated with the molecular methods are with (red diamonds) and without (black solid circles) augmentation corrections. All shieldings are absolute (valence only).

and (e) demonstrate that also for this molecule the augmentations have small, noticeable effects (diamonds). The current (direct) and D_{ij}-augmentation (converse) again yield identical corrections. Note that the corrections depend on the PAW data set.

Figure 10 shows the convergence with the kinetic energy cutoff on the KS orbitals (for the direct method). For the C, N, and O shieldings, good results are still obtained with a 600 eV cutoff, but even a cutoff as low as 400 eV could be used as the deviations are just a few ppm and to a large extent just linearly dependent on the σ_{iso}. For the hydrogen shieldings, their small range requires higher accuracy, so a cutoff of 400 eV is insufficient. The dependence of the isotropic shielding on cutoff is generally stronger for nuclei that are located at larger distance from the origin. This is a manifestation of the gauge problem discussed in Sec. III A 2. This error is only dominant, i.e., noticeable for the H shieldings.

For optimal computational speed, all calculations of the shieldings can be started from well-converged KS orbitals and corresponding Kohn-Sham potential as obtained without any moment or field applied. For the converse method, the optimal setting is an external moment of 100 μ_B, and 10 iterations[39]
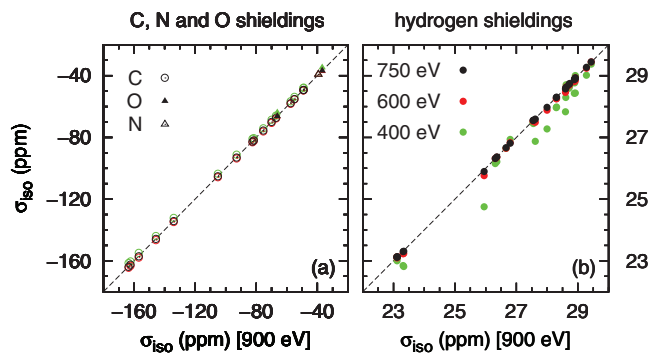

FIG. 10. Cutoff dependence of shieldings for the venlafaxine molecule using the direct (molecular) method. Abscissa: isotropic shieldings calculated with 900 eV kinetic energy cutoff. Ordinate: isotropic shieldings calculated with 400, 600, and 750 eV cutoffs (see legend). All shieldings are absolute (valence only).

per nucleus per direction. At a 900 eV cutoff, then for each nucleus it takes ~17 min to converge the shielding tensor on a single Intel Xeon L5520 processor (using 8 cores). With these settings carbon and hydrogen shieldings are converged better than 0.01 ppm, and O and H better than 0.1 ppm. For the direct method attaining convergence requires a bit more effort in general. For an external field of 100×10^{-6} $\mu_B/\text{Å}^3$, 10 iterations are sufficient to obtain a convergence better than 0.01 ppm for H and of ~0.1 ppm for C, O, and N.

For completeness Table VIII compares to available experiment.[40] Only C shieldings of the solid state system have been measured. Although our molecule is in vacuum, it still has the conformation of the molecules in the crystalline

TABLE VIII. Carbon isotropic shieldings of venlafaxine free base. Linear response (LR) and converse VASP results were obtained with 900 eV kinetic energy cutoff. QE denotes QUANTUM-ESPRESSO. All columns are referenced to their average. The bottom line reports the mean absolute deviation from experiment.

|	Expt.[a]	LR	LR	Converse		QE
Aug.		No	No	No	Yes	No
Geom.	Cryst.	Cryst.	Mol.	Mol.	Mol.	Mol.
8	−60.0	−60.88	−61.45	−61.44	−62.01	−62.58
9b	−56.1	−56.46	−54.66	−54.65	−55.00	−55.49
10b	−44.8	−45.06	−43.44	−43.43	−43.80	−44.21
11	−85.3	−86.30	−87.18	−87.17	−87.83	−88.36
10a	−34.8	−32.76	−31.87	−31.86	−31.95	−32.44
9a	−58.5	−59.71	−60.08	−60.08	−60.46	−60.95
5	22.0	21.36	19.64	19.65	19.62	19.63
4	−1.2	−4.46	−2.96	−2.96	−3.21	−2.44
3b	36.7	37.71	35.10	35.12	35.43	35.49
2b	51.1	52.24	52.97	52.98	53.44	53.65
1	46.1	46.74	47.25	47.26	47.65	47.89
2a	51.6	51.74	53.27	53.28	53.61	53.92
3a	42.8	45.12	44.51	44.52	44.80	44.91
6	11.6	11.66	9.35	9.35	9.38	9.49
7b	30.7	32.20	32.30	32.31	32.42	32.82
7a	26.5	26.53	26.78	26.73	27.05	27.33
12	20.8	20.33	20.47	20.40	20.88	21.34
MAE	0.0	1.0	1.6	1.6	1.7	1.8

[a]Reference 40.
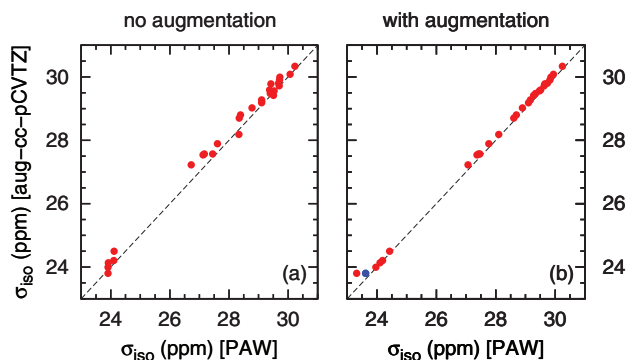
FIG. 11. Absolute isotropic hydrogen shieldings for the venlafaxine molecule. Abscissa: VASP isotropic shieldings calculated with 900 eV kinetic energy cutoff. Ordinate: GIAO aug-cc-pCVTZ isotropic shieldings calculated with DALTON. VASP shieldings have been extrapolated to infinite cell size (0.8 ppm correction). Blue dot: VASP shielding with hard O PAW data set.

polymorph I. In order to enable a comparison, we reference the experimental and the various calculated C shieldings to their average (i.e., all columns in the table have average 0). For a linear response calculation on the full crystal geometry, the mean-average-error compared to experiment is 1.0 ppm. For calculations on the molecule in vacuum it increases to 1.6 ppm. Indeed, from the table it is evident that deviations between both geometries are small throughout and that agreement with experiment is very good, i.e., allowing to clearly assign the shieldings to the correct nuclei. A possible exception are C 2a/2b that have nearly degenerate shieldings. The a/b assignments are based on theory only. All other assignments could be made in Ref. 40. The augmentation corrections do not improve agreement with experiment here. However, they are negligible anyway for C.

The importance of augmentation corrections is again evident for the hydrogen shieldings. In Fig. 11 the GIPAW isotropic shieldings are compared to quantum-chemical GIAO results obtained with DALTON and an aug-cc-pCVTZ basis set. Without augmentation applied, there is some scatter (left panel). The scatter is largely removed when the two-center augmentation corrections are included (right panel); the data points are on a nearly straight line, except for a single point at the lower end of the shielding range. This point pertains to a hydrogen bonded to oxygen. All the other hydrogens are bonded to carbon. For this single hydrogen, the two-center corrections are particularly large. The situation resembles the H_2O test from Sec. IV B, where a fortuitous agreement disappears when augmentation is applied. Using the hard oxygen data set of Sec. IV B improves the results also here (blue dot). The difference in shifts for this point is reduced to 0.2 ppm. Further improvement might result from an optimized PAW O data set or a more complete quantum-chemical basis set. However, calculations at the aug-cc-pCVQZ level for this molecule are already very demanding.

V. CONCLUSION

We present two simple finite-field implementations for the calculation of chemical shieldings specifically for molecules using a periodic supercell approach and a plane-wave basis set in first-principles DFT. One is a direct method, mimicking to a large extend the actual NMR experiment, the other is of the novel class of converse methods. Both approaches have a GIPAW reconstruction of the shape of the KS valence orbitals in the region near the core to obtain good accuracy. The direct approach is conceptually very simple, and relies on the application of a saw-tooth shaped field.

We have discussed (gauge related) basis-set (in)completeness and finite size effects. The implementation was validated using several (small and large) molecules, containing also a "difficult" nucleus such as phosphorous. Particular emphasis was put on hydrogen shieldings, as these are relatively more sensitive to small errors.

We go beyond previous GIPAW implementations in two respects: (a) We include two-center contributions to the shieldings. For hydrogen this noticeably improves the accuracy. (b) The converse GIPAW approach is generalized to non-norm-conserving PAW.

The simplicity of, in particular, the direct approach makes it easy to implement in any PAW plane wave code. As a linear response calculation is avoided, it should be easier to generalize to post-DFT methods in principle (also an advantage of any converse method, see Ref. 18).

Although the converse approach is more demanding on computational resources in principle, as calculations need to be repeated for each nucleus, we expect it to be useful anyway. It is a bit more robust in convergence and can have a minimal E_{cut} (no gauge problems). For zooming-in on a specific part of a large molecule (e.g., near an active site) it could be the method of choice. Otherwise the direct method is preferable. Both are less-involved than a full-scale GIPAW linear response calculation.

ACKNOWLEDGMENTS

[1]W. G. Proctor and F. C. Yu, Phys. Rev. **77**, 717 (1950).
[2]W. C. Dickinson, Phys. Rev. **77**, 736 (1950).
[3]T. Helgaker, M. Jaszuński, and K. Ruud, Chem. Rev. **99**, 293 (1999).
[4]F. Mauri, B. G. Pfrommer, and S. G. Louie, Phys. Rev. Lett. **77**, 5300 (1996).
[5]D. Sebastiani and M. Parrinello, J. Phys. Chem. A **105**, 1951 (2001).
[6]T. Gregor, F. Mauri, and R. Car, J. Chem. Phys. **111**, 1815 (1999).
[7]C. Pickard and F. Mauri, Phys. Rev. B **63**, 245101 (2001).
[8]P. E. Blöchl, Phys. Rev. B **50**, 17953 (1994).
[9]R. Ditchfield, Mol. Phys. **27**, 789 (1974).
[10]J. R. Yates, C. J. Pickard, and F. Mauri, Phys. Rev. B **76**, 024401 (2007).
[11]T. Charpentier, Solid State Nucl. Magn. Reson. **40**, 1 (2011).
[12]D. Skachkov, M. Krykunov, E. Kadantsev, and T. Ziegler, J. Chem. Theory Comput. **6**, 1650 (2010).

[13]D. Skachkov, M. Krykunov, and T. Ziegler, Can. J. Chem. **89**, 1150 (2011).

[14]R. Laskowski and P. Blaha, Phys. Rev. B **85**, 035132 (2012).

[15]T. Thonhauser, D. Ceresoli, A. Mostofi, N. Marzari, R. Resta, and D. Vanderbilt, J. Chem. Phys. **131**, 101101 (2009).

[16]D. Ceresoli, T. Thonhauser, D. Vanderbilt, and R. Resta, Phys. Rev. B **74**, 024408 (2006).

[17]Note that the Kronecker deltas in Eq. (2) of Ref. 15 can be understood to arise from the interaction energy $-\mathbf{m}^{ext} \cdot \mathbf{B}^{ext}$. Here this energy is excluded from E.

[18]D. Ceresoli, N. Marzari, M. Lopez, and T. Thonhauser, Phys. Rev. B **81**, 184424 (2010).

[19]P. Giannozzi, S. Baroni, N. Bonini, M. Calandra, R. Car, C. Cavazzoni, D. Ceresoli, G. L. Chiarotti, M. Cococcioni, I. Dabo, A. Dal Corso, S. de Gironcoli, S. Fabris, G. Fratesi, R. Gebauer, U. Gerstmann, C. Gougoussis, A. Kokalj, M. Lazzeri, L. Martin-Samos, N. Marzari, F. Mauri, R. Mazzarello, S. Paolini, A. Pasquarello, L. Paulatto, C. Sbraccia, S. Scandolo, G. Sclauzero, A. P. Seitsonen, A. Smogunov, P. Umari, and R. M. Wentzcovitch, J. Phys.: Condens. Matter **21**, 395502 (2009).

[20]G. Kresse and J. Hafner, Phys. Rev. B **48**, 13115 (1993).

[21]G. Kresse and J. Furthmller, Comput. Mater. Sci. **6**, 15 (1996).

[22]T. Thonhauser, D. Ceresoli, and N. Marzari, Int. J. Quantum Chem. **109**, 3336 (2009).

[23]C. M. Gowda, F. Vasconcelos, E. Schwartz, E. R. H. van Eck, M. Marsman, J. J. L. M. Cornelissen, A. E. Rowan, G. A. de Wijs, and A. P. M. Kentgens, Phys. Chem. Chem. Phys. **13**, 13082 (2011).

[24]DALTON, a molecular electronic structure program, Release 2.0, 2005, see http://www.kjemi.uio.no/software/dalton/dalton.html.

[25]K. Wolinski, J. F. Hinton, and P. Pulay, J. Am. Chem. Soc. **112**, 8251 (1990).

[26]T. Helgaker, P. Wilson, R. Amos, and N. Handy, J. Chem. Phys. **113**, 2983 (2000).

[27]G. Kresse and D. Joubert, Phys. Rev. B **59**, 1758 (1999).

[28]R. D. King-Smith, M. C. Payne, and J. S. Lin, Phys. Rev. B **44**, 13063 (1991).

[29]In their linear response method YPM remove this gauge problem with the f-sum rule (Ref. 10).

[30]J. Mason, Solid State Nucl. Magn. Reson. **2**, 285 (1993).

[31]We calculate the core shielding using the atom's core orbitals and Eq. (27) of Ref. 18.

[32]J. P. Perdew, K. Burke, and M. Ernzerhof, Phys. Rev. Lett. **77**, 3865 (1996).

[33]J. P. Perdew, K. Burke, and M. Ernzerhof, Phys. Rev. Lett. **78**, 1396 (1997).

[34]Oxygen is at $(x, y) = (-0.76681, 0.59378)$, the hydrogen nuclei are at $(0, 0)$ and $(-1.53362, 0.00000)$. All positions are in Å.

[35]Same number of projectors per ℓ channel, same core radii.

[36]Six molecules: P_2, P_4, PH_3, P_2H_4, PF_3, and H_3PO_4. The structures were optimized with VASP in the gas phase approximation and used for all different methods.

[37]Or the carbon, nitrogen, and oxygen positions we use the experimental data for polymorph I obtained with XRD in Ref. 40. Hydrogen positions have been optimized at the PBE level.

[38]Jmol: an open-source Java viewer for chemical structures in 3D, see http://www.jmol.org/.

[39]Iterations in VASP settings: NELM = 10.

[40]J. T. M. van Eupen, W. W. Elffrink, R. Keltjens, P. Bennema, R. de Gelder, J. M. M. Smits, E. R. H. van Eck, A. P. M. Kentgens, M. A. Deij, H. Meekes, and E. Vlieg, Cryst. Growth Des. **8**, 71 (2008).